Master's Thesis of Engineering

Wind Load and Structural Response Assessment of High-Rise Building Using Computational Fluid Dynamics

전산유체역학을 이용한 초고층 건물의 풍하중과 풍응답 산정에 관한 연구

February 2023

Graduate School of Engineering

Seoul National University

Architecture and Architectural Engineering

Han Sol Lee

Wind Load and Structural Response Assessment of High-Rise Building Using Computational Fluid Dynamics

Advisor: Thomas Kang

Submitting a Master's thesis of
Architecture and Architectural Engineering

February 2023

Graduate School of Engineering
Seoul National University
Architecture and Architectural Engineering
Han Sol Lee

Confirming the Master's thesis written by
Han Sol Lee

February 2023

Chair	Sung-Gul Hong	(Seal)
Vice Chair	Thomas Kang	(Seal)
Examiner	Cheol-Ho Lee	(Seal)

Abstract

Wind Load and Structural Response Assessment of High-Rise Building Using Computational Fluid Dynamics

Lee, Han Sol

Department of Architecture and Architectural Engineering

College of Engineering

Seoul National University

Computational fluid dynamics (CFD) is a strong tool to simulate the wind flow around the building. Due to the improvement of computer performance and CFD models, efficiency of CFD in the usage of building design has increased.

In this study, assessment of wind load using the CFD simulation on high-rise building was carried out. Simulated wind pressure field was compared with the wind tunnel test result, using spectral analysis and modal analysis to verify if CFD successfully simulates the aerodynamic characteristic of wind flow around the building. A case study of the time history analysis of high-rise building was conducted using obtained wind loads from CFD and wind tunnel

tests. Design wind load evaluated from the peak response using both wind tunnel test and CFD was compared. Then, potential of CFD as the revising tool for wind tunnel test with a lack of pressure taps was discussed. To check if the integration of fluctuating wind pressure obtained by CFD shows the same trends with wind tunnel test result, its characteristic was discussed in terms of correlation and integrated power spectrum. Finally, effects of different selection of wind pressure taps on the wind load assessment were discussed using both results from wind tunnel tests and CFD.

Keywords: Computational Fluid Dynamics, Wind Load, High-Rise Building.

Student Number : 2021-25117

Contents

List of Tables

List of Figures

Chapter 1. Introduction

1.1 Motivation of research

Wind load is one of the most dominant components of lateral load on tall building. Due to the cantilever effect and spectral characteristic, wind load becomes more critical as the building gets higher. Because of highly dependent characteristic of wind load on the shape of the building and its uncertainty, experimental analysis for the assessment of wind load is often required. Currently, wind tunnel test is the most favorable method for assessing the wind load on the building. However, wind tunnel tests has limitations in terms of cost of wind tunnel equipment and scaled model of building.

Computational fluid dynamics (CFD) is a numerical tool for simulating the wind flow around the building. CFD has an advantage in regard to the potential of controlling multi-parameters and detailed observation for every location. While finite element method is a major tool for structural analysis, CFD may not be a major method in wind load assessment due to its uncertainty on the accuracy and its high computational cost. Recently, demand of computational cost is decreasing due to the improvement of computer performance and theoretical development, but uncertainty on the accuracy is a remaining problem.

In this study, assessment of wind load and response on the high-rise building is conducted using CFD. Simulated wind pressure field on the building is compared with that from wind tunnel test to validate its performance. Case studies on the wind response of high rise buildings is conducted, and peak response and corresponding design wind load are assessed.

Even though CFD is still somewhat unreliable and computationally cost-

expensive, possibility of CFD as a supporting tool of wind tunnel test can be discussed. Currently high-frequency force balance test (HFFB) which measures the base overturning moment is a most common method for wind tunnel test, but high-frequency pressure integration test (HFPI) which measures the wind pressure using the pressure tap on the building is also widely used due to its potential in more specified analysis and advantage in usage for façade design. However, equipment for HFPI test such as synchronous channel or scaled building model is costly, and error of integrated wind load due to the lack of the number of pressure taps can occur. In this study, characteristic of wind pressure integration is analyzed and the effect of pressure tap selection on the integrated wind load is discussed by comparing CFD and wind tunnel test results.

1.2 Scope and objective

The main purpose of this study is to evaluate the wind load and response on the high-rise building using CFD and verify its usage as the assessment tool for wind design. Also, potential of CFD as the revising tool of wind tunnel test was discussed to redeem the limitation of the high frequency pressure integration test of wind tunnel test.

1.3 Organization

This thesis consists of six main chapters. Chapter 1 introduces the scopes and organization of this study. Background and literature review of CFD and wind load assessment are shown in Chapter 2. Chapter 3 consists of CFD setup and simulated wind pressure field on the high-rise building. Structural response of building to the obtained wind load from CFD and evaluated equivalent static wind load are discussed in Chapter 4. Chapter 5 investigates the characteristic of integration of wind pressure to wind load and effects of the pressure tap location on the assessment of wind load using CFD. The conclusion is summarized in Chapter 6.

Chapter 2. Background and Literature Review

2.1 Open-access wind tunnel test

Because the wind load is random process by the fluctuation of wind by eddies, full time history data of wind tunnel test is rarely available from prior research. Instead, representative properties of wind load such as mean and variance, or spectral functions such as PSD or coherence is commonly discussed in researches. Fortunately, there are some available open-access wind tunnel test data. Tokyo Polytechnic University (TPU) provides a set of open-access wind tunnel test data (Tamura, 2012).

TPU aerodynamic database provides wind tunnel test data of the isolated tall building with rectangular plan. High-frequency pressure integration test (HFPI) was conducted for the rectangular plan building. Length scale 1/400 was used for the test and two types of power law exponent 1/4 and 1/6 were used for the wind profile. **Table 2-1** shows the wind tunnel test cases provided by TPU aerodynamic database. For each case, total 32.768 second data was obtained with 1000 frequency sampling ratio. HFPI test for every case was repeated with 11 different wind incident angles from 0° to 50° with 5° interval.

For scaled model of building, uniform pressure tap distribution with 0.02m distance between pressure taps was used. For building case with aspect ratio of 5 and square plan, five pressure taps were located in row and 25 pressure taps in column, which results in total 500 pressure taps on the building surface. For each pressure taps, time history of wind pressure coefficient with mean wind velocity at the building height is provided.

TPU aerodynamic database also provides HFPI test data for cases with two buildings located close to each other to discuss the interference effect of surrounding buildings. Also, HFPI test data for gable roofed low-rise building

is provided with both isolated case and interfered case by surrounding buildings. In this study, only the isolated high-rise building case is analyzed.

Table 2-1 Wind tunnel test cases of isolated building in TPU aerodynamic database

D (mm)	B (mm)	H (mm)	Power law exponent
100	100	100	1/4 and 1/6
		200	
		300	
		400	
		500	
	200	200	1/4
		300	
		400	
		500	
	300	200	1/4 and 1/6
		300	
		400	
		500	

2.2 Computational fluid dynamics

2.2.1 Governing equation and turbulence model

Computational fluid dynamics (CFD) is numerical tool for evaluating the movement of fluid. CFD computes the wind using two governing equation. Two governing equations are continuity equation, which is about conservation of mass, and the Navier-Stokes (NS) equation which is about conservation of momentum.

Direct Numerical Simulation (DNS) is a simulation method of CFD by directly solving two governing equations. For wind flow with high Reynolds number, DNS can easily fail and high computational cost is required due to high frequency fluctuation and turbulence dissipation on molecular viscosity. To overcome this problem, two turbulence model is used to simplify the dissipation of turbulence energy at high frequency. Two most general models are Reynolds Averaged Navier-Stokes (RANS) and Large Eddy Simulation (LES).

RANS estimates the turbulence effect using additional equation. Most general type of RANS model are the k-epsilon model and k-omega SST model. A problem of RANS is that it can only solve the time-averaged result. Fluctuating component such as variance of fluctuating pressure cannot be directly obtained by RANS, and fluctuations should be modeled using additional models. There are an improved model of RANS, which is the Unsteady RANS (U-RANS), but it still can solve the large scale fluctuations and small scale eddies need some approximation.

LES directly computes the eddies larger than the mesh size with governing equation, and estimates the eddies smaller than the mesh size using the filter. Time-dependent components such as time series of wind load can be obtained by LES, but much higher computational cost is required compared to RANS. LES has strength in creating time history data of wind load, but because LES cannot directly calculate the small eddies, it usually underestimates the high-frequency component of wind load depending on the mesh size.

Figure 2-1 shows the distribution of solved range of turbulence by RANS, LES, and DNS (Tamura and Kareem, 2013). While DNS can cover the most of the frequency range, LES cannot evaluate the turbulence at inertia region where the eddies are smaller than the mesh size of simulation. RANS can only simulate the large scale fluctuation, so RANS could be effective for simulating the dominant phenomena and physics of wind, but it cannot be used for research with higher complexity such as obtaining time history wind load and assessment of design wind load.
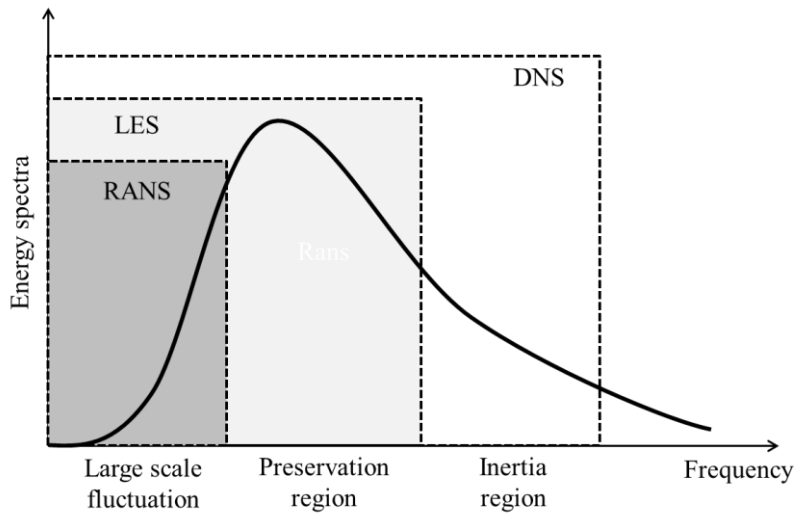
Figure 2-1 Solved range of CFD by RANS, LES, and DNS (Tamura, 2013)

2.2.2 Application of CFD in wind design

Figure 2-2 shows the procedure suggested by Tamura *et al.* (2008) for estimating the wind loads on building using CFD. For RANS, it can only obtain mean wind pressure on the building. For this case, gust effect factor which represents the ratio between peak wind load and mean wind load is used to estimate the peak wind load. Wind pressure obtained by LES includes the time history data, so it can be directly used for spectral modal analysis or time history response analysis.
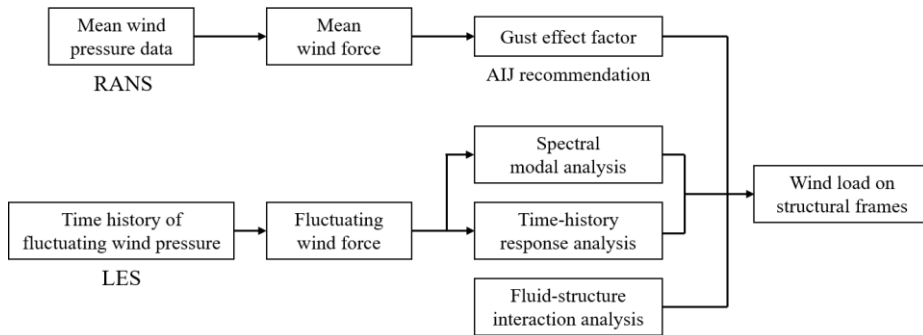
Figure 2-2 Procedure of estimating wind load on building using CFD (Tamura, 2008)

For application of LES in wind design of building, several case studies were conducted by previous studies. But currently most of studies focus on the peak wind pressure on the building for façade design, and only few studies with consideration of peak wind load by structural analysis exists. Ricci *et al.* (2018) conducted LES on the high-rise building and compared the result with wind tunnel test, and showed error up to 30%, which was insufficient accuracy for structural design. Thordal *et al.* (2020) conducted framework of LES on the CAARC standard high-rise building and resulted in the accuracy within 20% error for peak wind pressure coefficient and 13% for peak wind response. Most of studies concluded that accuracy of LES depends on the mesh refinement and accuracy of incident wind profile.

LES with fine mesh can show responsible performance, but the remaining problem is computational cost of LES. Even though computational time depends on the mesh resolution and computer performance, still most of

16

researches spent around 100h for single simulation. Since Korea Design Standard (KDS) 41:2022 requires at least 32 wind directions for wind tunnel test, currently application of LES on wind design is ineffective.

2.3 Assessment of peak wind load and response

Wind load on the building is composed of mean, background, and resonant component. Mean and background component can be directly evaluated from the wind load, but assessing the effect of resonant component requires evaluation of structural response.

Because of the difficulty of defining the dynamic fluctuations of wind load and difficulty of dynamic analysis, concept of equivalent static wind load is used for the design wind load of building in codes and standards. Equivalent static wind load is the static load corresponding to the peak wind response obtained by dynamic wind load.

To assess a peak wind load from time history obtained by experiment, directly using the maximum value is not appropriate because of its uncertainty. To consider uncertainty, peak factor is used to evaluate the peak wind load. Peak factor represents the ratio between the standard deviation and differentiation between peak and mean. For most codes including KDS, Davenport peak factor (Davenport, 1964) is used. However, Davenport's method have limitations that it approximates the Gaussian distribution. However, actual distribution of wind load on building is non-Gaussian and closer to Gumbel distribution.

For peak factor for non-Gaussian distribution, Peng *et al.* (2014) compared the methods proposed before. In large scheme, Gumbel method and Translation method are most common methods. Gumbel method assumes the distribution as Gumbel distribution and find the peak. Translation method uses translation function to fit the original distribution to the Gaussian distribution.

Chapter 3. CFD Simulation on the Building

In this chapter, CFD simulation on the isolated building was conducted, and the result was compared with the test result from wind tunnel test. Based on the wind pressure, integrated load and power spectral density was compared with the wind pressure from the wind tunnel test. To check if CFD successfully simulates the aerodynamic characteristic of wind load, modal decomposition was conducted to specify the characteristic of the fluctuating pressure field on the building.

3.1 Simulation setup

3.1.1 Simulation setup and computational domain

CFD simulation was conducted for comparison of wind load assessment by CFD and wind tunnel test. CFD simulation for the building with square section and aspect ratio 5 was conducted with wind incident angle of 0, 15, 30, and 45 degrees, and wind tunnel test data from TPU aerodynamic database is used for comparison. For each simulation, total 12.5 seconds was simulated with 25,000-time steps of 0.0005 second interval. Size of the time step was decided based on the Courant number. Courant number is the ratio of mesh size and fluid movement in single time step, which is expressed by

$$C = \frac{U \Delta t}{\Delta h} \tag{3-1}$$

where C is Courant number, U is fluid velocity, and Δt, Δh is size of time step and length of mesh. Courant number is recommended to be below 1 so that wind flow don not skip the mesh cell between the time step. In this study, time step was decided as 0.0005s to satisfy this condition.

Computational domain for CFD simulation was decided base on the AIJ recommendation (2008) and COST guideline (2011). **Figure 3-1** and **Table 3-1** show the computational domain and its mesh region of CFD simulation. Inlet and outlet of the domain is located each 5H and 15H distance from the target building which H is the height of the building. Width and height of the domain is each 10H and 4H. For meshing method, cutcell method is used for the meshing method, where hexahedron mesh is used and mesh size is doubled as region changes. Total domain is divided into five regions, and building surface with deepest region was divided into 32 meshes in width and depth, and 160 meshes in height. Overall, total 7.01 million meshes was used for simulation.

Because the wind flow is unstable at the start of the simulation, first 5.0 sec among the total simulated time was removed for the stabilization and later 7.5 sec simulation was used for further analysis. With time scale 1/80, obtained 7.5 sec simulated data corresponds to 10-minute data with 0.04 s time step in real scale.

For data collection, total 1900 points were predefined on the building with 25 rows and 19 columns in each face for simultaneous wind pressure data. 500 points among those points are in the same location with the pressure taps used in the wind tunnel test by TPU aerodynamic database. **Figure 3-2** shows the distribution of predefined points for CFD and pressure tap locations used in the wind tunnel test.
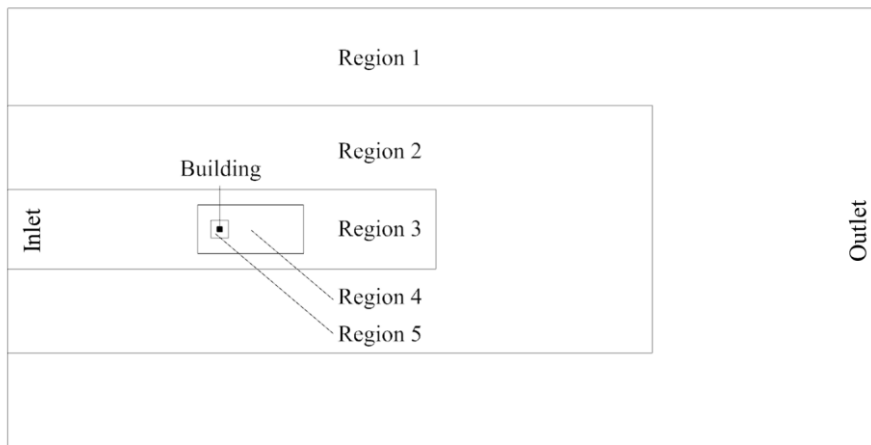
Figure 3-1 Computational domain of CFD simulation

Table 3-1 Size of mesh region and mesh size

Region	Region size	Mesh size (length)
1	20H×10H×4H	B/2
2	15H×6H×3H	B/4
3	10H×2H×2H	B/8
4	2.4H×1H×1.5H	B/16
5	0.4H×0.4H×1.1H	B/32
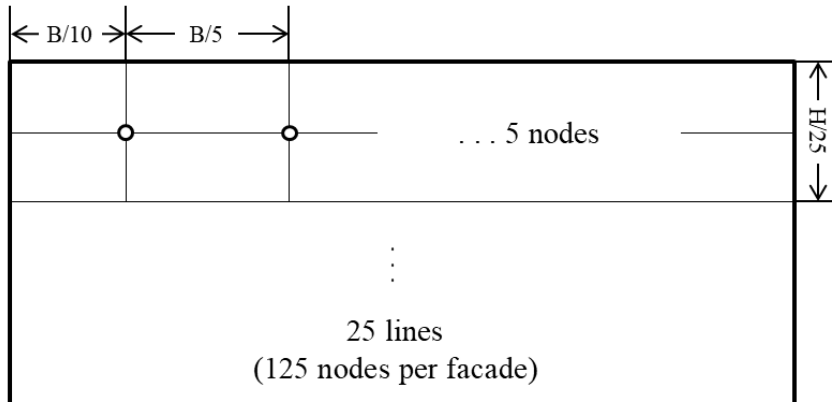
(a) Pressure tap distribution for WTT
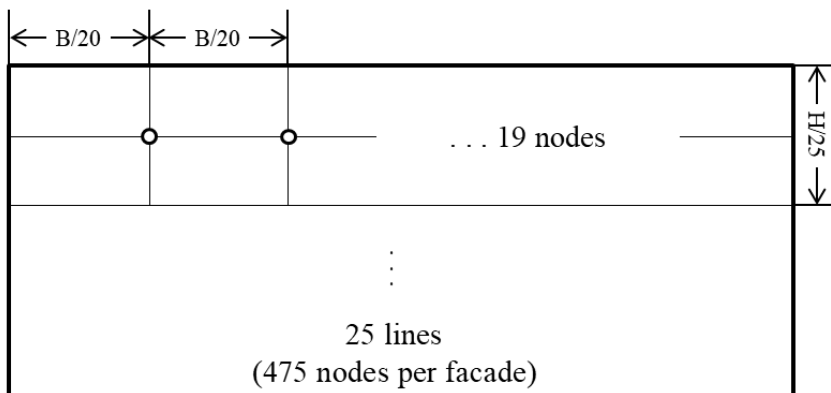
(b) Pressure tap distribution for CFD

Figure 3-2 Pressure tap distribution on building for WTT and CFD

3.1.2 Inlet wind specification

To compare the result obtained by CFD and wind tunnel test, same mean velocity and turbulence intensity with the wind tunnel test of TPU aerodynamic database with power law exponent 1/4 was used for wind profile. Because the turbulence length scale is not provided in TPU aerodynamic database, turbulence length scale suggested in the design code KDS 41:2022 was used with length scale 1:400 for simulation. **Table 3-2** shows the summary of the target wind profile.

Table 3-2 Target wind profile

Property	Target profile
Mean velocity	$V(h) = 11.14(h/H)^{0.25}$ (m/s)
Turbulence intensity	$I(h) = 11.16(h/H)^{-0.3}$ (%)
Turbulence length scale	$L(h) = \begin{cases} 0.25\left(\dfrac{H}{0.075}\right)^{0.5} & 0.075m < H \\ 0.25 & H \le 0.075m \end{cases}$ (m)

Because the wind profile of inlet flow and incident flow on building is different due to development of turbulence, inlet wind profile was adapted with CFD simulation in the empty domain. Initial simulation in the empty domain without building was done with target wind profile in the inlet. Then, inlet wind profile was adapted based on the difference of the inlet and incident flow. **Figure 3-3** shows the target, adapted, and two incident wind profile. For incident wind on building, Incident 1 is the wind profile when the inlet wind has same profile with target wind, and Incident 2 is the wind profile when adapted profile is applied in inlet. As shown in the figure, wind velocity remains stable with wind development, but the turbulence intensity shows large difference with inlet and incident wind.

Figure 3-3 Wind profile of target, adapted profile for inlet and incident wind

3.2 Wind pressure field comparison

3.2.1 Comparison of wind pressure

For wind tunnel test data (WTT) from TPU aerodynamic database, total 32.7 seconds wind pressure data was divided into 4 parts with 7.5 seconds for the ensemble averaging. With time scale 1/400, 7.5 s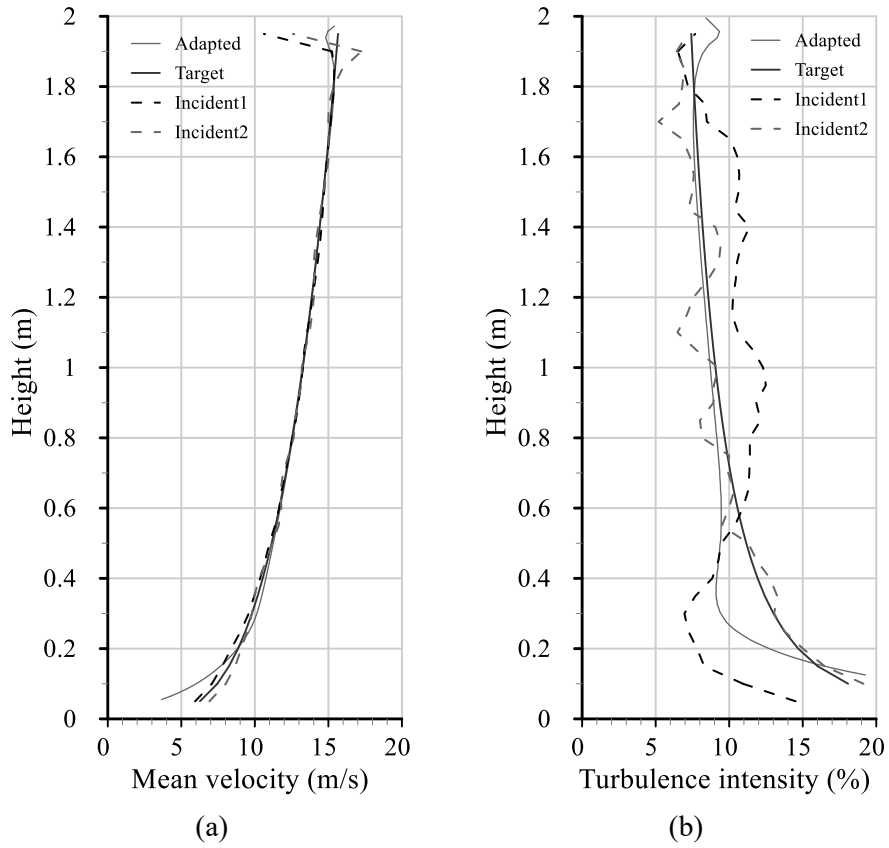econds data corresponds to the 10-minute data in real scale. For CFD, only single 7.5 seconds data is obtained for each wind incident angle, so ensemble averaging was not conducted.

To compare the wind pressure on the building, wind pressure coefficient is widely used to normalize the wind pressure using following equation.

$$C_P = \frac{q}{0.5\rho V_H^2} \tag{3-2}$$

where C_P is the wind pressure coefficient, q is wind pressure, ρ is the density of air, and V_H is the wind velocity at building height.

Figure 3-4 and **3-5** shows the contour plot of wind pressure coefficient field determined by WTT and CFD with comparison of mean and standard deviation. α_W is the wind incident angle for labels of each plot. For mean wind pressure coefficient, overall scheme of contour plot showed good agreement, but usually overestimation of positive pressure and underestimation of negative pressure was found.

For standard deviation of wind pressure coefficients, WTT and CFD showed some different schemes. For every cases, CFD showed unusual pressure at the corner of sidewall where the vortex shedding by flow separation occurs. To overcome such problem, smaller meshes is recommended. WTT and CFD result also showed difference for standard deviation of wind pressure coefficient at windward wall. While WTT data shows a gradually decreasing fluctuation as height decrease, fluctuation for CFD data showed an increasing tendency at lower height. This seems to be CFD overestimating the effect of downwash.
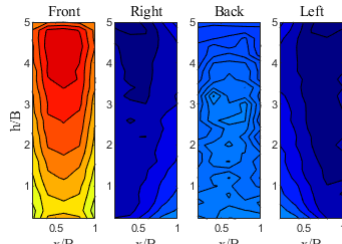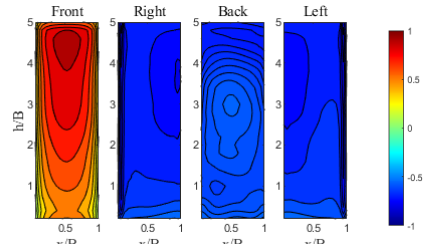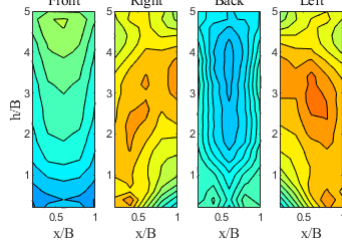
(a) Mean - $\alpha_W = 0°$ - WTT   (b) Mean - $\alpha_W = 0°$ CFD

(c) Fluctuating - $\alpha_W = 0°$ - WTT   (d) Fluctuating - $\alpha_W = 0°$ - CFD
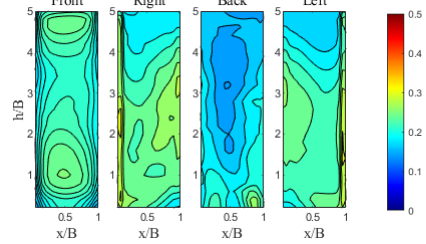
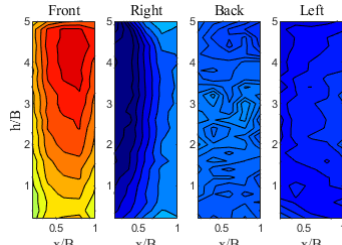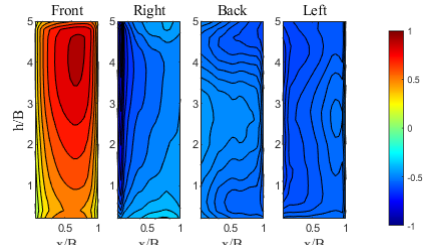(e) Mean - $\alpha_W = 15°$ - WTT   (f) Mean - $\alpha_W = 15°$ - CFD

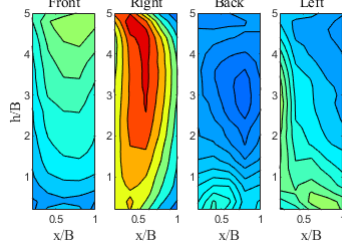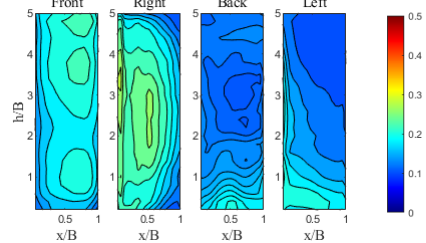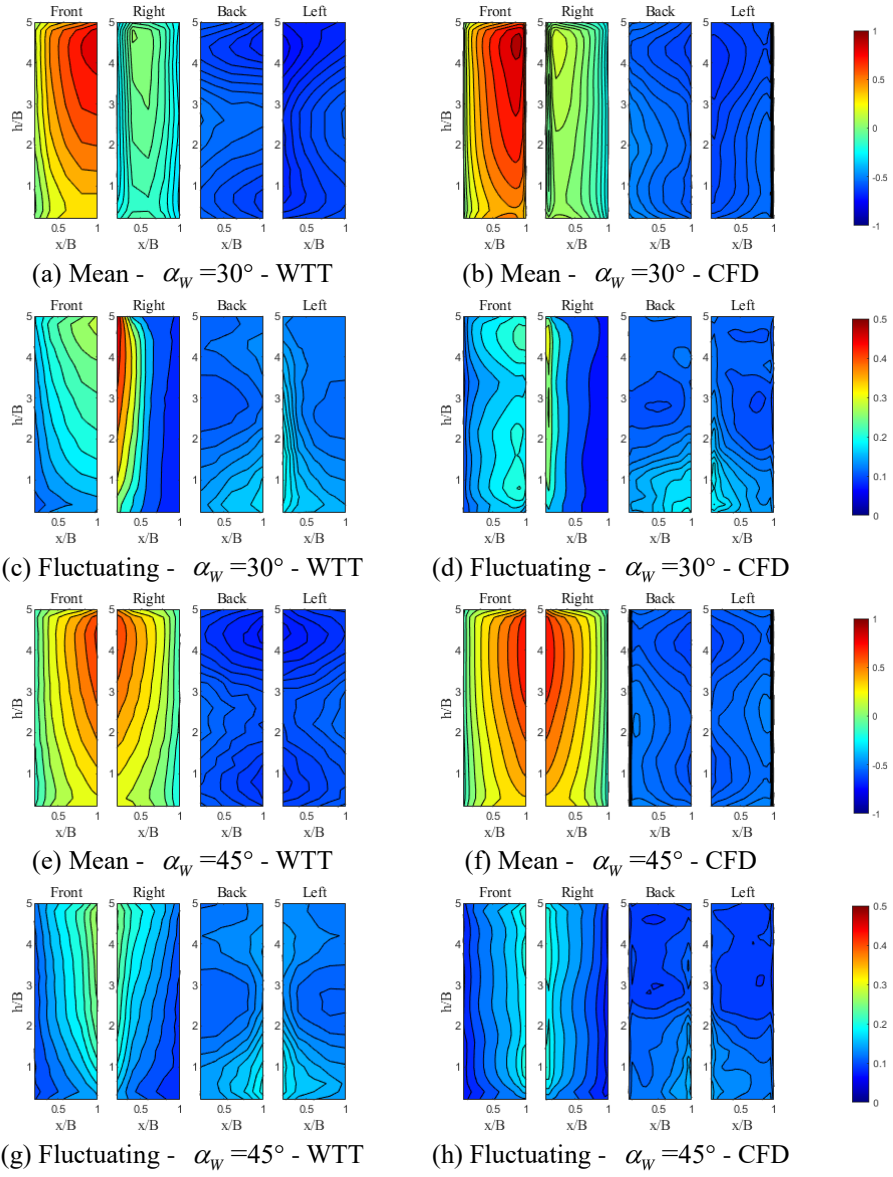(g) Fluctuating - $\alpha_W = 15°$ - WTT   (h) Fluctuating - $\alpha_W = 15°$ - CFD

**Figure 3-4** Contour plot of wind pressure coefficient for wind incident angle 0° and 15°

26

Figure 3-5 Contour plot of wind pressure coefficient for wind incident angle 30° and 45°

Figures 3-6 and **3-7** show the scatter plot of comparison of wind pressure field at 500 points with location of pressure tap used in WTT. For mean wind pressure, usually overestimation on the windward side and underestimation on the sidewall and leeward side was found for CFD result. Standard deviation showed similar tendency for WTT and CFD, but overall underestimation was found for CFD result. Most of the error occurred at the sidewall which was affected by the vortex shedding.

While mean and fluctuating wind pressure showed similar result for WTT and CFD, skewness and kurtosis did not show clear agreement. For adjustment of skewness and kurtosis, probability density of wind velocity might be needed to control. Current spectral synthesizer method used for turbulence generation only uses the property of turbulence intensity and turbulence length scale for the turbulence generation, so probability density function of the generated wind cannot be controlled. For accuracy of skewness and kurtosis, alternative method for turbulence generation must be discussed or longer development length from the inlet of CFD domain to the building is needed so that wind follows the behavior of wind in wind tunnel test.
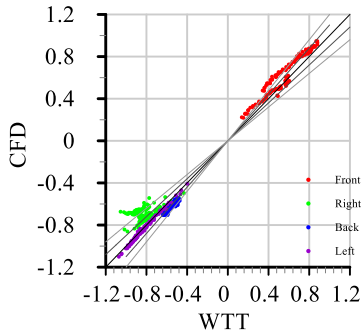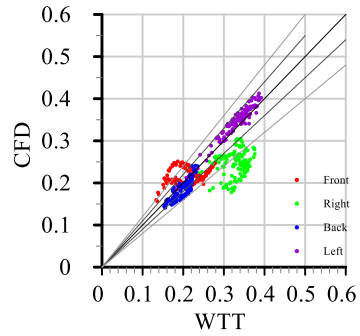
(a) Mean - Wind angle 0° (b) Fluctuating - Wind angle 0°
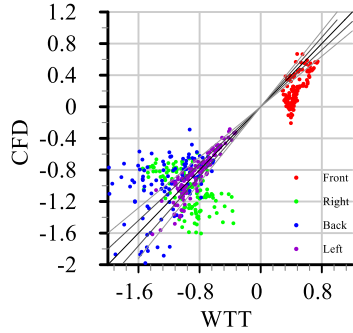
(c) Skewness - Wind angle 0° (d) Kurtosis - Wind angle 0°
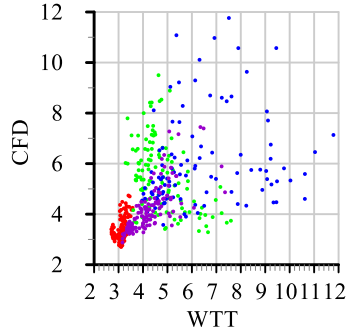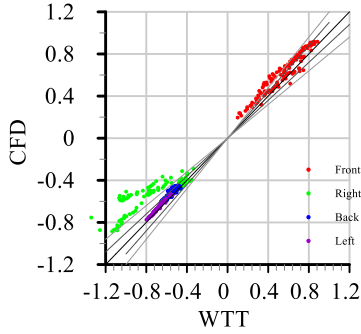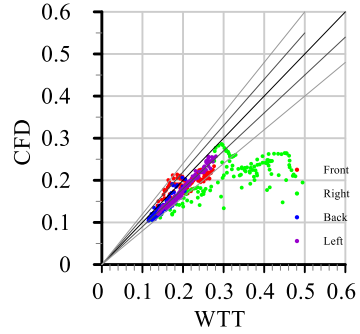
(e) Mean - Wind angle 15° (f) Fluctuating - Wind angle 15°
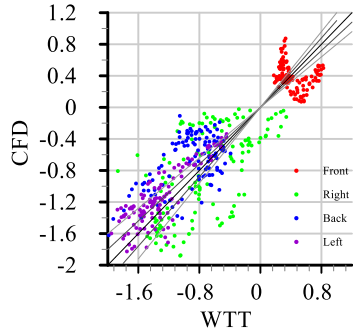
(g) Skewness - Wind angle 15° (h) Kurtosis - Wind angle 15°
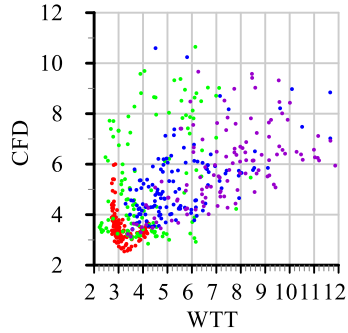
Figure 3-6 Scatter plot of comparison of wind pressure by CFD and WTT for wind incident angle 0°, 15°

(a) Mean - Wind angle 30°

(b) Fluctuating - Wind angle 30°

(c) Skewness - Wind angle 30°

(d) Kurtosis - Wind angle 30°

(e) Mean - Wind angle 45°
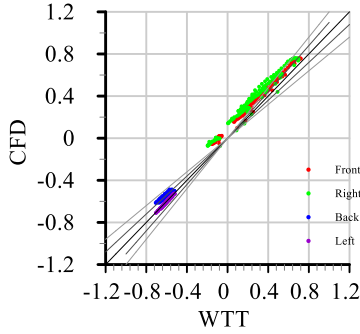
(f) Fluctuating - Wind angle 45°
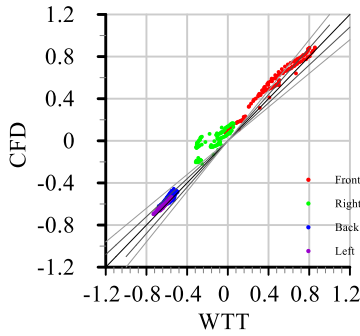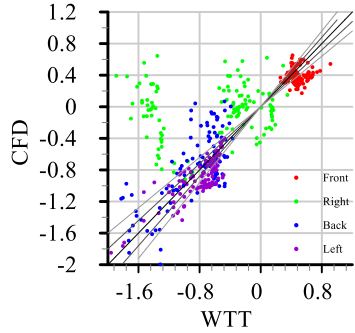
(g) Skewness - Wind angle 45°
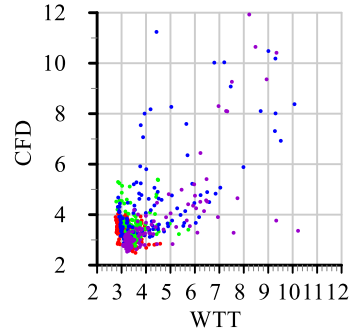
(h) Kurtosis - Wind angle 45°

Figure 3-7 Scatter plot of comparison of wind pressure by CFD and WTT for wind incident angle 30°, 45°

3.2.2 Comparison of integrated wind load

With integrating wind pressure in pressure taps with its tributary area, wind load on each height of the building and base overturning moment can be obtained. Force and overturning moment of wind load can be normalized using following equations.

$$C_{F_i} = \frac{F_i}{0.5\rho V_H^2 B} \tag{3-3}$$

$$C_{M_i} = \frac{M_i}{0.5\rho V_H^2 B H^2} \tag{3-4}$$

$$C_{F_t} = \frac{F_t}{0.5\rho V_H^2 B^2} \tag{3-5}$$

$$C_{M_t} = \frac{M_t}{0.5\rho V_H^2 B^2 H} \tag{3-6}$$

where F_i is wind load per height, M_i is base overturning moment, and C_{F_i} and C_{M_i} are wind force coefficient and wind moment coefficient, respectively. Equation (3-3) and (3-4) are for along- and across-wind load, respectively, and Equation (3-5) and (3-6) are for torsional wind load. From the wind pressure field, mean and fluctuating integrated wind load can be normalized in the same way.

Figure 3-8 and 3-**9** show the mean and standard deviation of integrated wind load with height for WTT and CFD, respectively. While along-wind and across-wind load showed good agreement with some error, torsional-wind load did not fit except for the wind incident angle 45°.

Figure 3-10 summarizes the moment coefficient of directional base overturning moment. For mean and fluctuating moment coefficient, CFD showed a similar tendency with WTT, but overall underestimation was found in CFD. For skewness and kurtosis, CFD showed a similar tendency with WTT except for the torsional wind load at wind incident angle 30°.
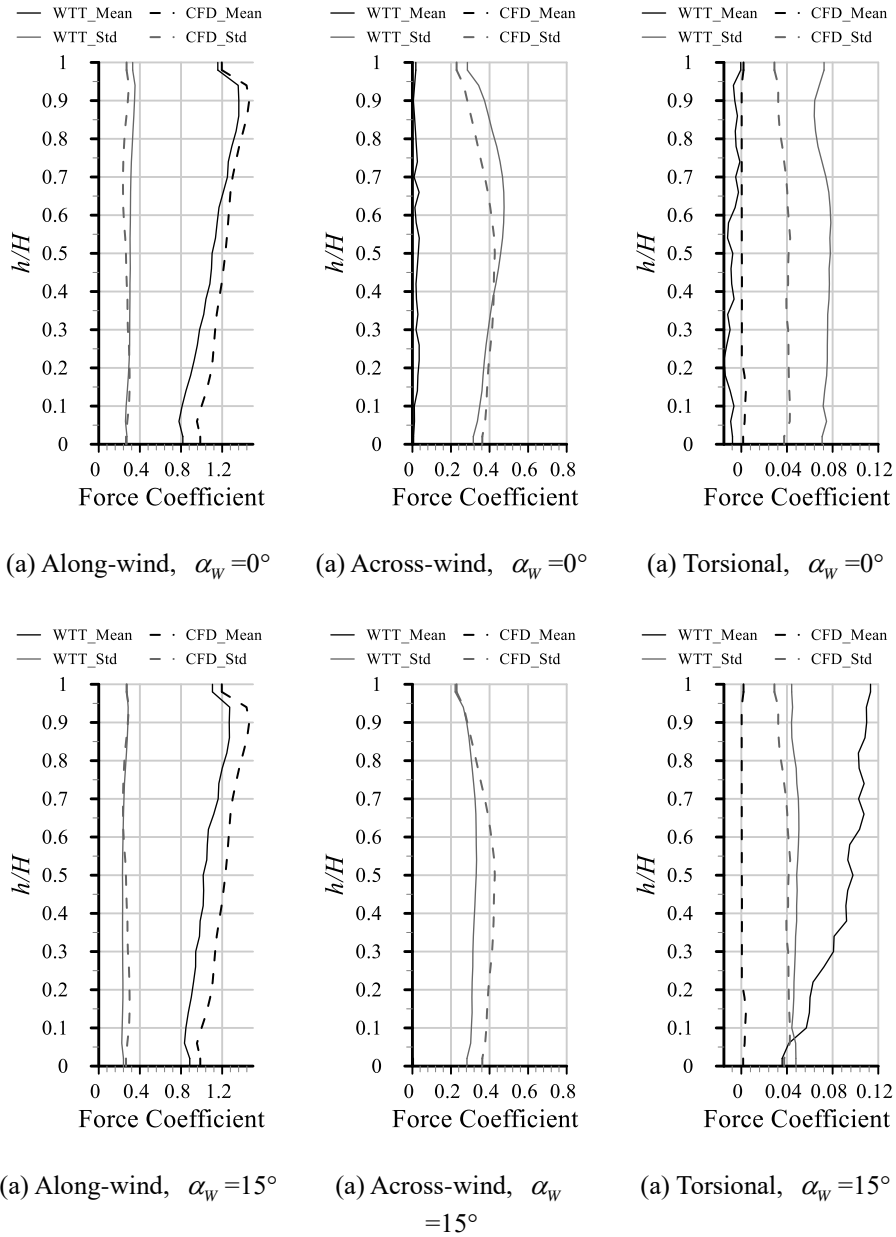
Figure 3-8 Wind load coefficient with height for wind incident angle 0° and 15°
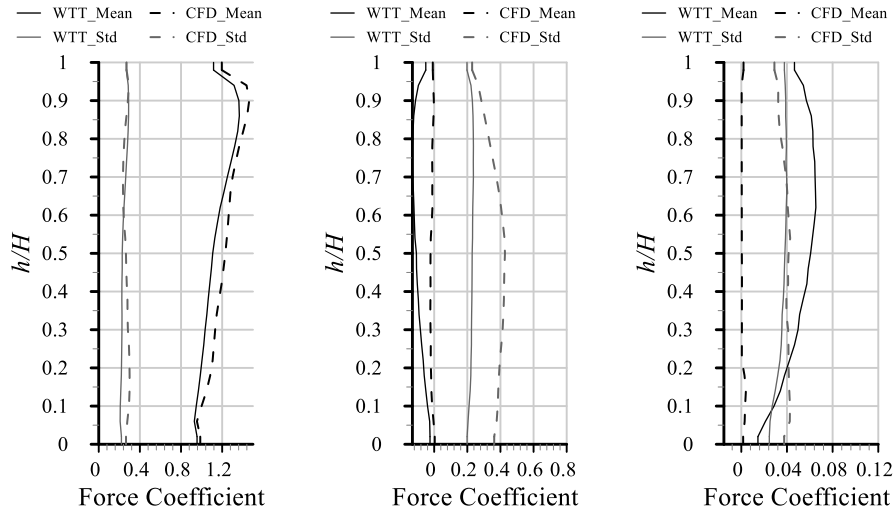
(a) Along-wind, α_W =30°   (a) Across-wind, α_W =30°   (a) Torsional, α_W =30°
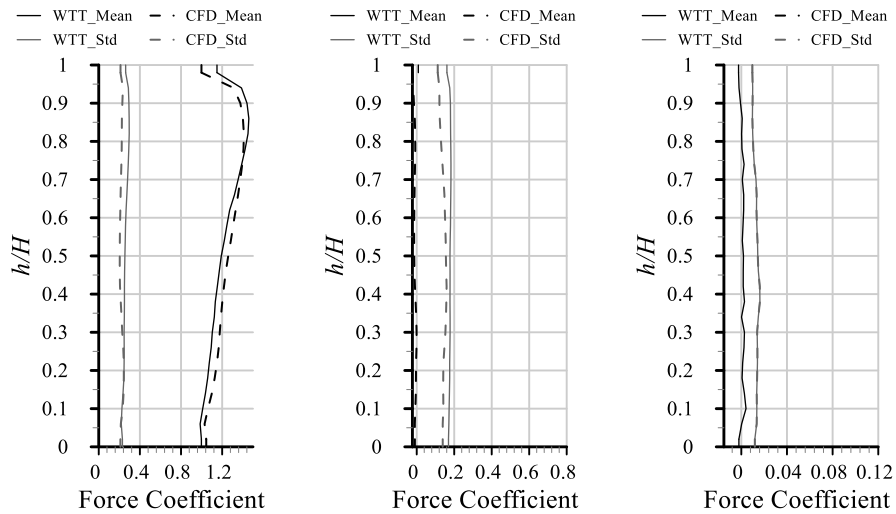
(a) Along-wind, α_W =45°   (a) Across-wind, α_W =45°   (a) Torsional, α_W =45°

Figure 3-9 Wind load coefficient with height for wind incident angle 0° and 15°
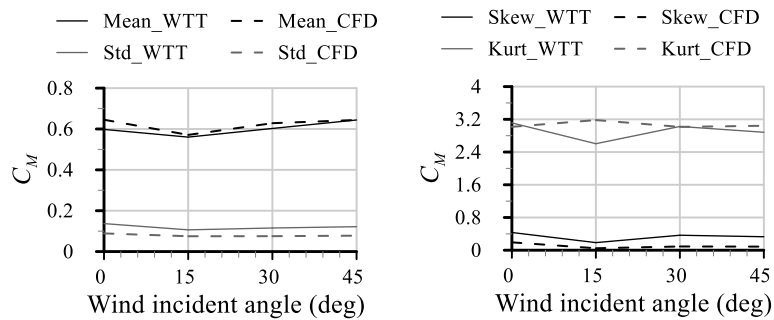
(a) Along-wind base OTM
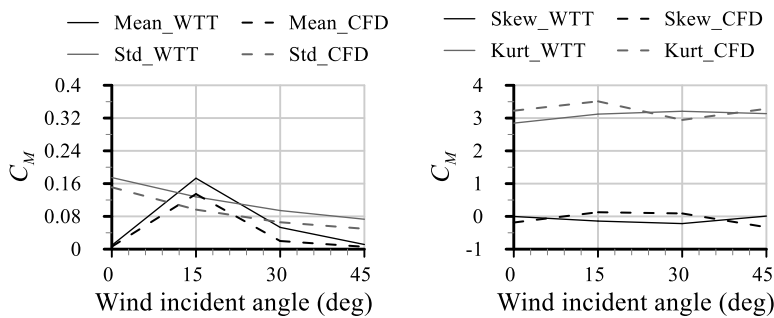
(b) Across-wind base OTM
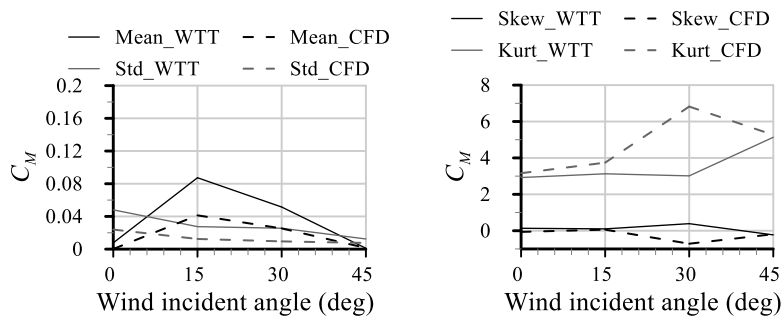
(c) Torsional-wind base OTM

Figure 3-10 Wind moment coefficient of base overturning moment

3.3 Spectral analysis of wind load

To analyze and compare the random process of fluctuating wind load, power spectral density (PSD) is widely used for both researches and design codes. PSD function represents the energy of fluctuating component at each frequency.

With same geometric ratio of building and wind property, usually spectral property of wind load shows similar tendency for different building size and wind velocity. To compare those cases with varying geometric size, normalized frequency and normalized PSD function is widely used. For normalized frequency, fL/V is usually used where L and V is representative length and velocity, respectively. In this study for analysis of wind load on building, width of building B and wind velocity at building height is used for representative length and velocity. PSD function is divided into variance of original function, which is equal with integration of the PSD function.

In KDS 41:2022, PSD function of the base overturning moment of along-, across-, and torsional-wind load is provided for the standard square-shaped building with wind incident angle 0.

Figures 3-11 and **3-12** compare the normalized PSD function of base overturning moment obtained by WTT and CFD. For case with wind incident angle 0°, PSD function provided by KDS 41:2022 was also compared. For along-wind PSD, WTT and CFD showed good agreement but did not fit with KDS 41:2022. For across-wind, Both WTT and CFD showed a clear peak for PSD at normalized frequency 0.1. This normalized frequency is called Strouhal number, which represents the periodic vortex shedding at the corner of the building. In comparison with KDS 41:2022, both WTT and CFD showed a higher contribution of low frequency domain in PSD compared to KDS 41:2022. For base torsional moment, effect of vortex shedding by flow separation and reattachment is represented in KDS 41:2022 as two local peaks, and similar tendency of local peaks was also found for both WTT and CFD.

Similar with wind incident angle 0, tendency of PSD for WTT and CFD also showed a good agreement for other cases. For most of the case, CFD showed

lower contribution of high frequency domain compared to WTT. This is because of the limitation of large eddy simulation, which underestimates the fluctuation of high frequency region. Because LES cannot directly calculate the eddy smaller than the mesh size, small eddies are estimated using the filter. To enhance the accuracy of PSD at high frequency region, smaller mesh size is required. Compared to the along- and across-wind, torsional-wind showed larger difference of PSD between CFD and wind tunnel test. This is due to the unstable result of CFD at the corner of building, which is also observed at the contour plot. Even though, the result shows that CFD is suitable to evaluate the PSD of wind load on the building.

(a) Along-wind, $\alpha_w = 0°$ (d) Along-wind, $\alpha_w = 15°$

(b) Across-wind, $\alpha_w = 0°$ (e) Across-wind, $\alpha_w = 15°$

(c) Torsional, $\alpha_w = 0°$ (f) Torsional, $\alpha_w = 15°$
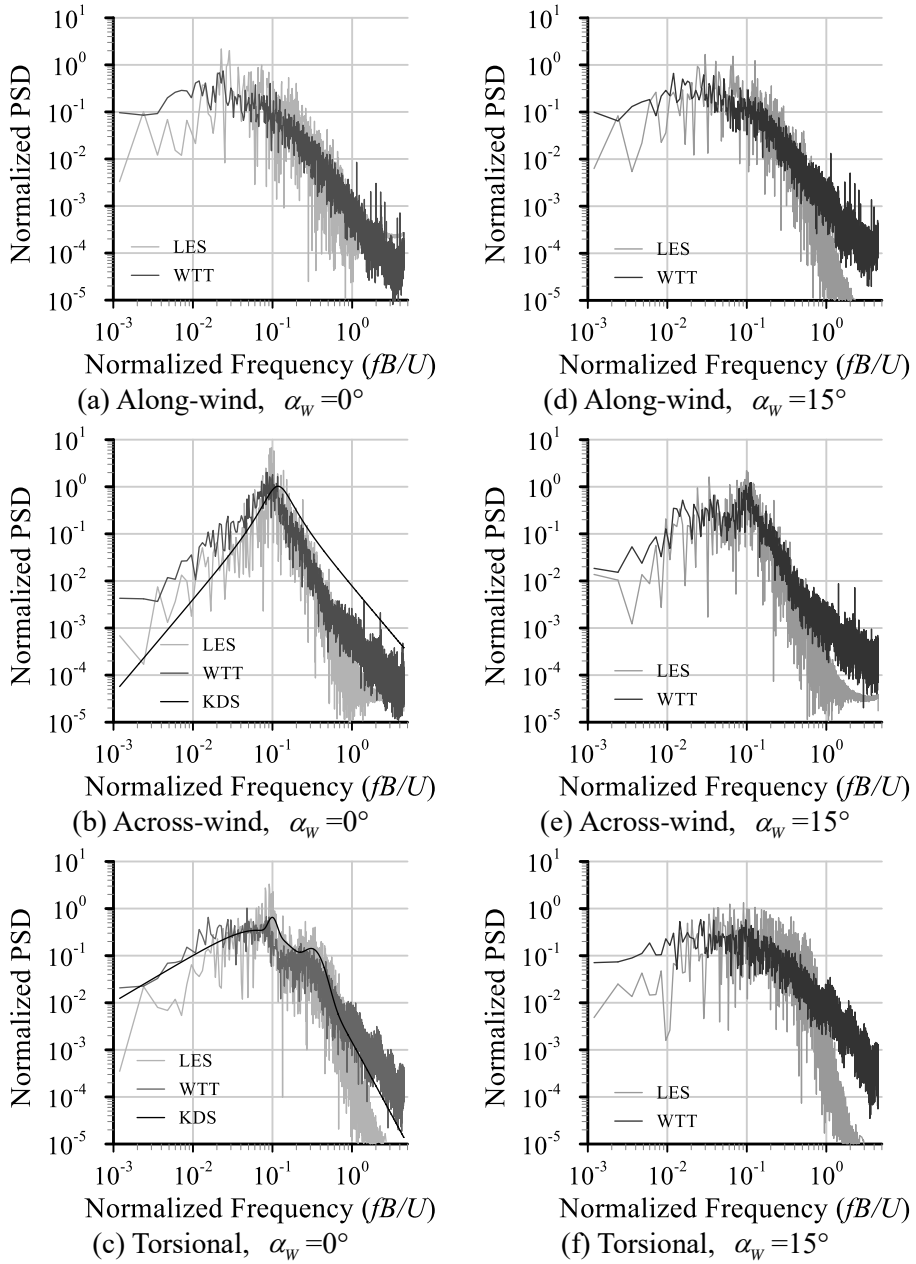
Figure 3-11 Normalized PSDs of base overturning moment with wind incident angle 0° and 15°
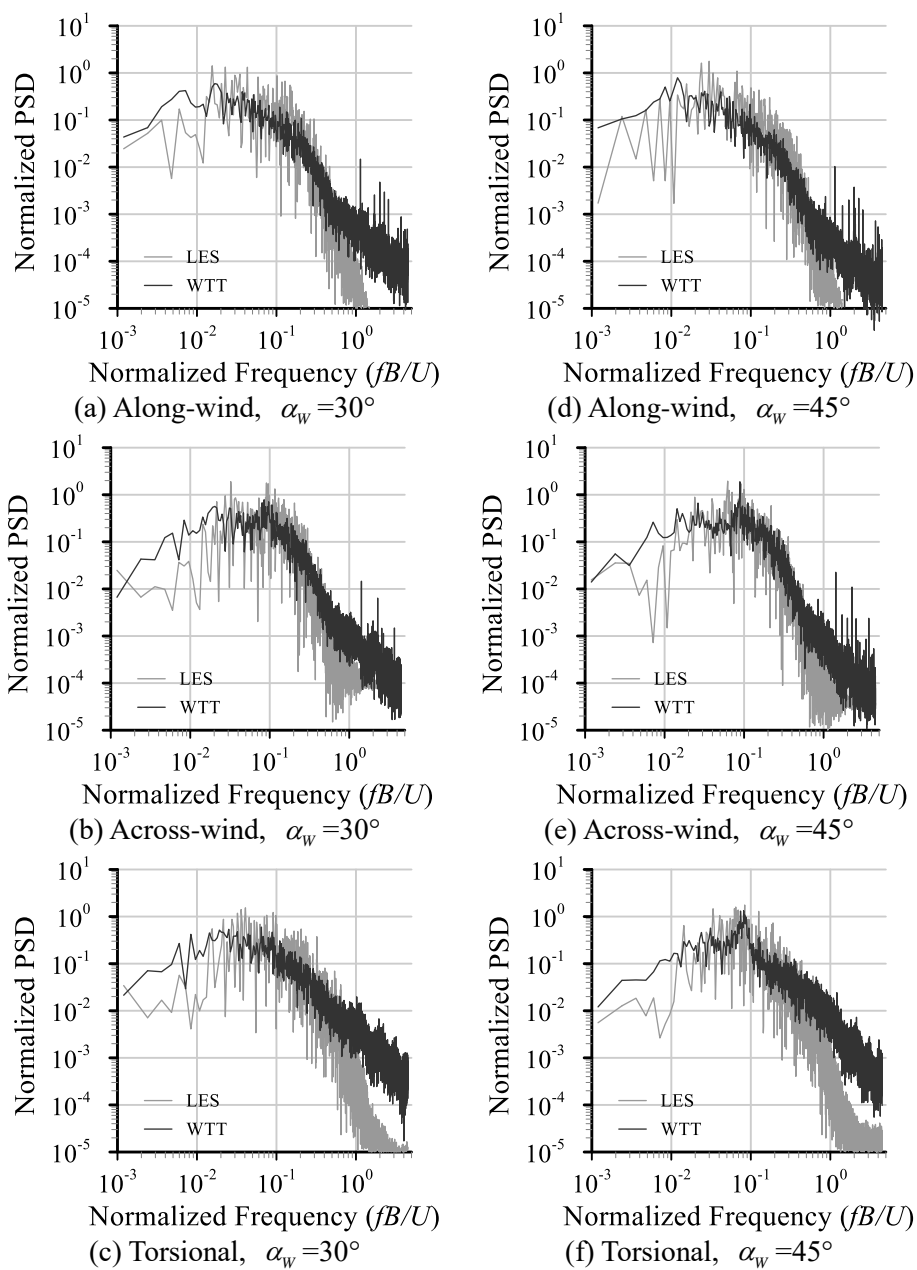
Figure 3-12 Normalized PSDs of base overturning moment with wind incident angle 30° and 45°

3.4 Modal comparison of wind pressure field

Because traditional analysis such as numerical analysis of mean and variance or spectral analysis is based on independent analysis of single fluctuating data, it cannot represent the characteristic of overall fluctuating feature of wind pressure field. To detect the pattern of fluctuating field, modal decomposition technique is used. To check if CFD simulates the appropriate aerodynamic feature of fluctuating wind pressure field, modal decomposition is applied to find the wind pressure pattern on the building for both CFD and WTT.

3.4.1 Proper orthogonal decomposition (POD)

Proper orthogonal decomposition (POD) is technique to decompose the fluctuating field into the optimal orthogonal coordinates. POD obtains the mode and its weight as the eigenvector and eigenvalue of the covariance matrix, respectively, as follows:

$$P_N = [X(t_1), X(t_2), ..., X(t_N)]$$ (3-7)

$$C = P^T P$$ (3-8)

where X is the original fluctuating field, P is the total snapshot of original fluctuating field and C is covariance matrix. Then, the eigenvector of covariance matrix becomes the POD mode ϕ. Eigenvalue corresponding to each POD mode represents the contribution of each mode on the total fluctuating field. From the POD modes, original fluctuating field can be reconstructed as follows:

$$X(t) = \sum a_j(t)\phi_j$$ (3-9)

where a is the modal coefficient which represents the fluctuation of POD mode.

Tamura *et al.* (1999) had applied POD to wind pressure field on a high-rise building and showed that a lower mode of POD could be explained as

physical phenomena such as vortex shedding or quasi-steady flow. Through POD analysis, contribution of each POD mode on the energy of fluctuation is obtained. Dominant modes with high contribution can be used to represent the phenomena of fluctuating wind pressure on the building.

POD analysis was applied to wind pressure field obtained by WTT and CFD. **Figure 3-14** shows the first three order POD mode shapes for wind incident angle 0°. For WTT, the first mode shows the effect of fluctuating incident wind, and the second and third mode show the effect of vortex shedding at the corner. In terms of integrated load, the first mode affects the fluctuating along-wind load and the second and third modes affect the across-wind load. Formation of the third mode is also related to the mean wind speed difference with the height, which the fluctuation of wind decreases with height. POD mode for CFD data showed similar result with WTT, but the order of the first and second mode was different.

Figure 3-15 shows the PSD of fluctuation of each POD mode. The first mode clearly shows the effect of turbulence of incident flow. The second and third modes of WTT and the first and third modes of CFD show peak at the frequency with Strouhal number, which shows the effect of vortex shedding at the corner of the building. Repetitive analysis was done for other wind incident angles, and WTT and CFD showed similar POD modes.

Figure 3-16 shows the correlation between the POD modes of WTT and CFD. Most of the modes have other modes with correlation higher than 0.6, but some modes with high correlation at other order of mode were captured. Even though CFD can simulate the phenomena of wind around the building, weight of each mode can be different with real-scale wind or wind tunnel test.
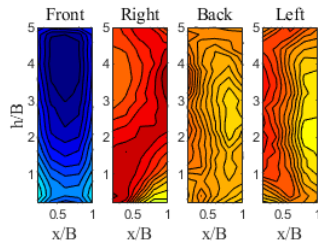
(a) 1st mode, WTT
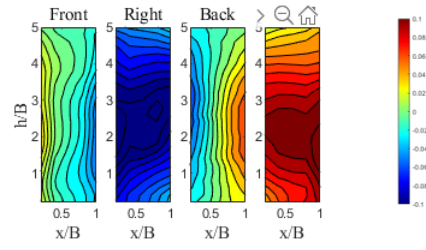
(b) 1st mode, CFD
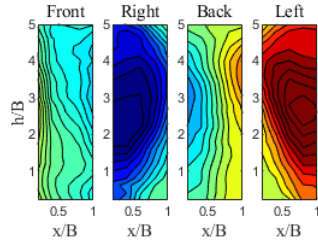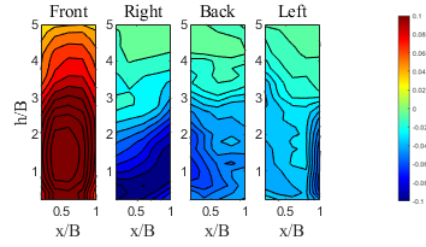
(c) 2nd mode, WTT
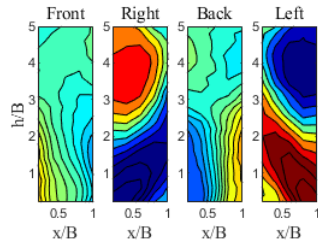
(d) 2nd mode, CFD
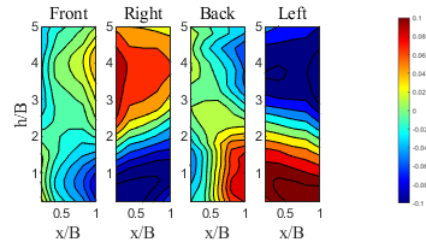
(e) 3rd mode, WTT

(f) 3rd mode, CFD

Figure 3-13 Three POD mode for wind incident angle 0°
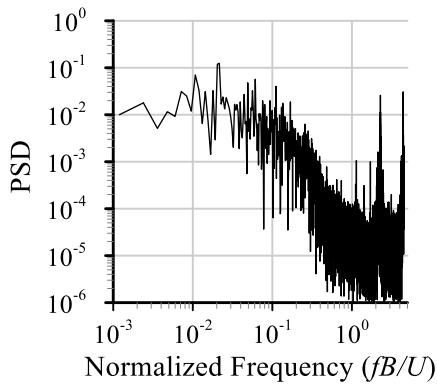
(a) 1st mode, WTT
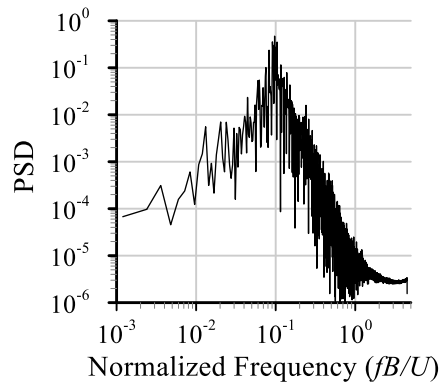
(b) 1st mode, CFD
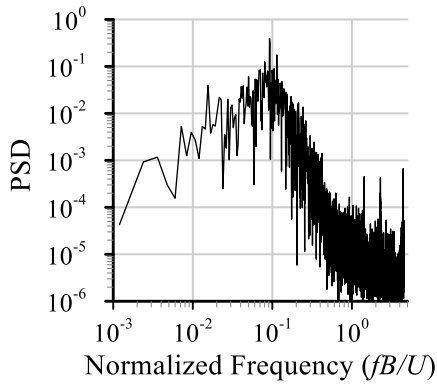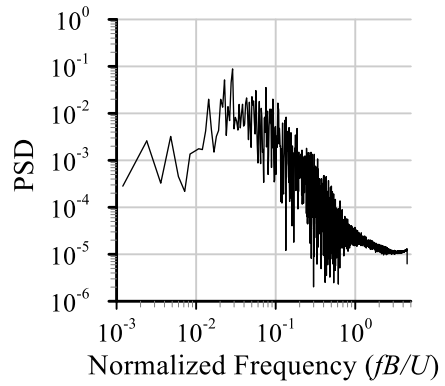
(c) 2nd mode, WTT
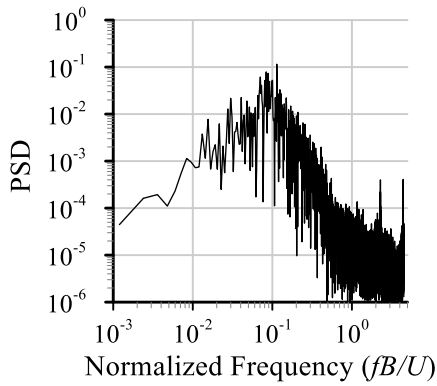
(d) 2nd mode, CFD

(e) 3rd mode, WTT
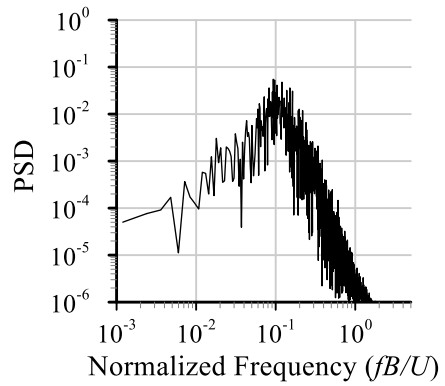
(f) 3rd mode, CFD

Figure 3-14 PSD of first two POD modes for wind incident angle 0°

42
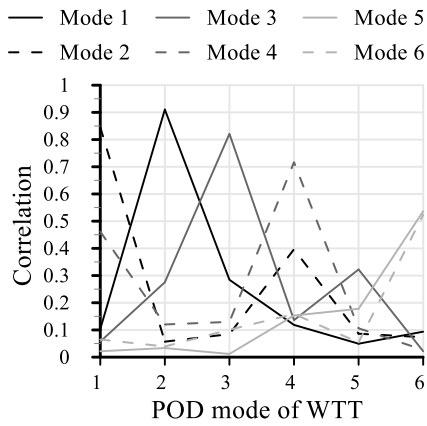
(a) Wind incident angle 0°
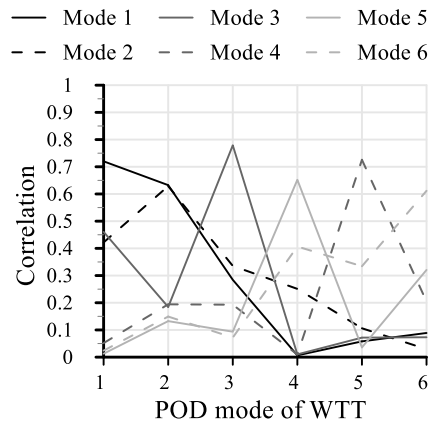
(b) Wind incident angle 15°
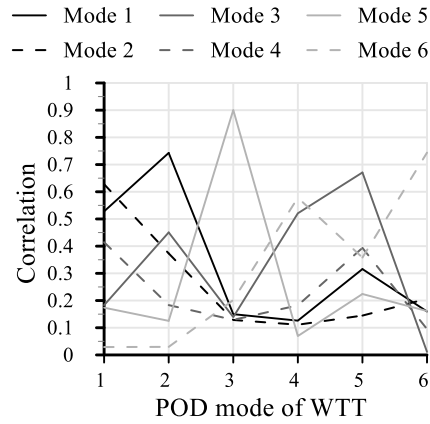
(c) Wind incident angle 30°
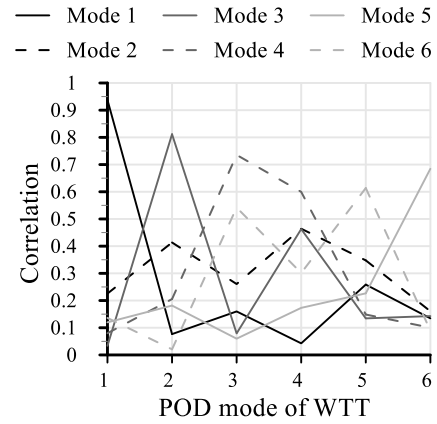
(d) Wind incident angle 45°

Figure 3-15 Correlation between POD modes of WTT and CFD

3.4.2 Dynamic mode decomposition (DMD)

Dynamic mode decomposition (DMD) is modal analysis based on Koopman operator, which is used to obtain a dynamic mode with temporal characteristic of fluctuating field (Schmid, 2010). While POD conducts the non-periodic mode with mixed frequency, DMD conducts the periodic mode with single fluctuating frequency and temporal growth or decay of amplitude. DMD obtains the mode based on the SVD decomposition of snapshot matrix to find the relation between different snapshots as follows:

$$P_{1:N-1} = U\Sigma W^T \tag{3-10}$$

where $P_{1:N-1}$ is snapshot from time step t_1 to t_{N-1}, U and W are orthogonal matrix, and Σ is diagonal matrix. Then, let $\Phi$ is eigenvector matrix of $U^T P_{2:N} W\Sigma^{-1}$, which shows the linear relation between two snapshot $P_{1:N-1}$ and $P_{2:N}$. Matrix of DMD modes is obtained as follows:

$$[\phi_1,...\phi_{N-1}] = P_{2:N} W\Sigma^{-1}\Phi \tag{3-11}$$

where ϕ is DMD mode.

From the obtained DMD modes and its initial amplitude and growth rate, original fluctuating field can be reconstructed by superposition of DMD modes as following:

$$X(t) = \sum \phi_k \exp(\Omega_k t)\alpha_k \tag{3-12}$$

where Ω and α are the growth rate and initial amplitude of each DMD modes, respectively. **Figure 3-16** shows the fluctuating amplitude of POD and DMD mode. For DMD mode, clear exponential growth or decay with fluctuation of uniform frequency is observed.

Luo and Kareem (2021) had applied DMD in the wind pressure field on the building and showed that DMD also could be used for detecting the pressure pattern by vortex shedding and aerodynamic phenomena of turbulence cascade of eddy from macro scale to micro scale. To evaluate the contribution

of each DMD mode on the fluctuating field, Kou and Zhang (2017) suggested the integration of amplitude of each DMD mode with total time domain to get the weight of each mode.

Figure 3-17 shows the scatter plot of normalized weights and fluctuating frequency of every DMD modes for WTT and CFD. For both data, local peak of weight at the Strouhal number is observed. Because the weight of each mode represents the energy at frequency domain, DMD modes of high frequency domain for CFD data showed lower weight compared to WTT due to the limitation on simulating small eddies.

Figure 3-18 shows the DMD modes at low frequency region with high weight and frequency with Strouhal number. Because not only single DMD mode represents the governing fluctuating scheme but similar DMD modes also exists in the surrounding frequency, DMD mode shape shows less significant feature than POD modes. Comparing with the POD modes in **Figure 3-13**, DMD mode at Strouhal number shows similar field with 2nd POD mode for WTT and 3rd POD mode for CFD data.

(a) Fluctuation of POD mode

(b) Fluctuation of DMD mode
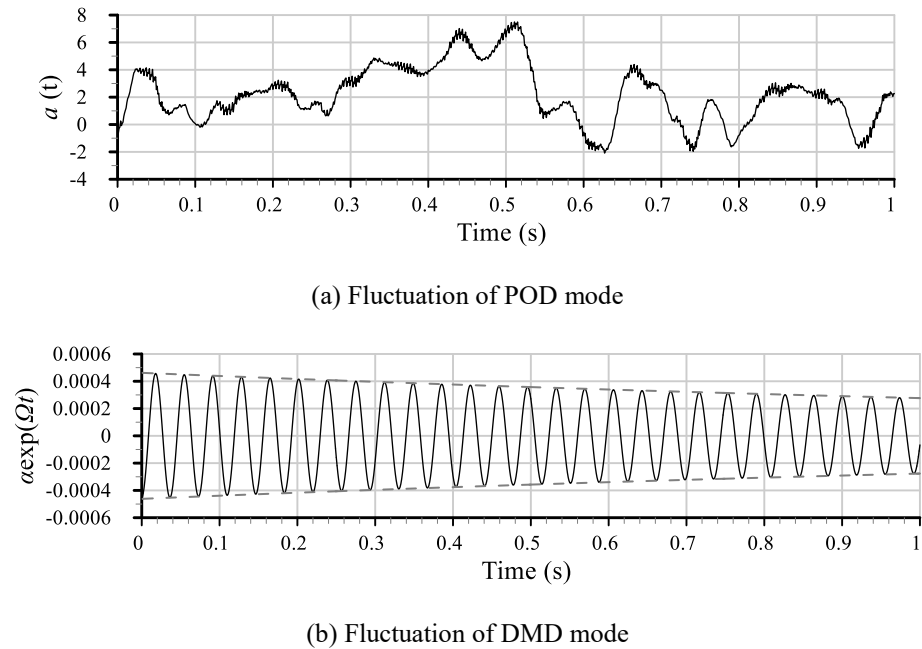
Figure 3-16 Fluctuation of POD mode and DMD mode
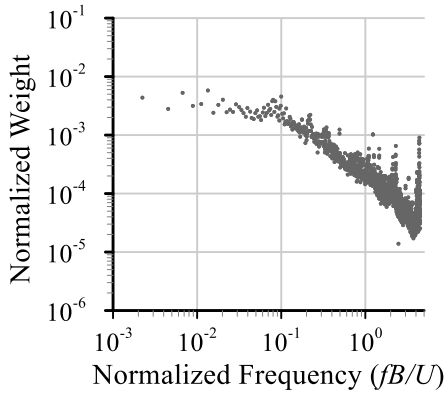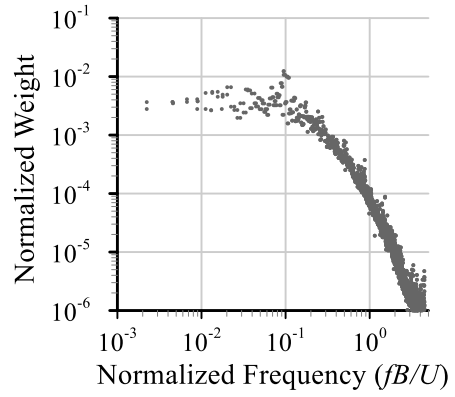
(a) WTT   (b) CFD

Figure 3-17 Contribution of DMD modes
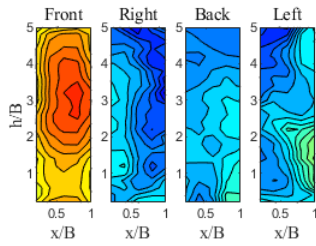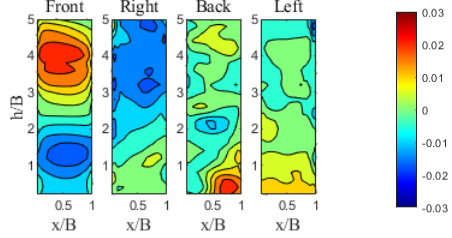
(a) fB/U=0.02, WTT   (b) fB/U=0.02, CFD
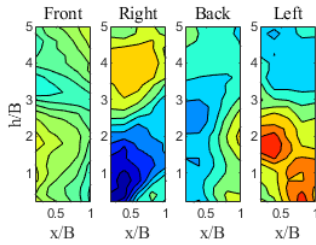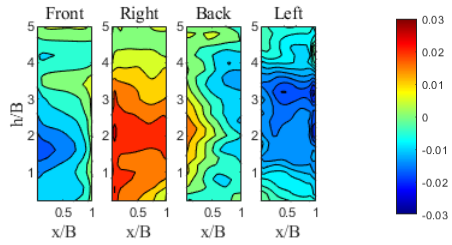
(c) fB/U=0.1, WTT   (d) fB/U=0.1, CFD

Figure 3-18 DMD mode shape at low frequency region and Strouhal number

3.5 Discussion

In this chapter, CFD simulation on the high-rise building with aspect ratio of 5 was conducted and the wind pressure field on the building was analyzed in comparison with the wind pressure obtained from wind tunnel test. Results are summarized as in the following.

(1) Mean and standard deviation of the wind pressure field evaluated by CFD showed good agreement with wind tunnel test, but skewness and kurtosis which is related to the probability distribution did not showed good agreement. For integrated wind load, overall underestimation of base overturning moment was found for CFD.

(2) Power spectral density of the directional wind loads showed good agreement between CFD and WTT. Due to the limitation of LES on the assumption of small eddies, underestimation of PSD at the high frequency region was captured.

(3) Modal decomposition by POD and DMD showed that CFD can successfully simulate the feature of fluctuating wind pressure field. For both CFD and WTT, first two POD modes usually represent the turbulence of incident wind and the vortex shedding at the corner. However, contribution and order of each mode showed some difference with wind tunnel test.

Chapter 4. Peak Wind Load and Response Assessment Using CFD

In this chapter, time history analysis of high-rise building using the wind load obtained from CFD and wind tunnel test was carried out. From the analysis, peak response and corresponding equivalent static wind load is evaluated. Error percentage of base overturning moment by CFD compared to wind tunnel test is obtained to check the applicable range of CFD.

4.1 Analysis building model

4.1.1 Structural Property

Wind load on the building is composed of mean, background, and resonance component. Unlike mean and background component, resonance component is highly affected by the building's structural property. Due to the effect of the resonance, structural response of building shows different scheme with the applied wind load. Thus, structural analysis is necessary for the assessment of peak wind load and response on the building. In this chapter, structural analysis on the high-rise building with height 200m was conducted. To apply the wind load obtained from the wind tunnel test and CFD, same geometric ratio for the case study building with square section and aspect ratio 5 was used. **Figure 4-1** shows the structural plan of the building used for case study. **Tables 6-1** and **6-2** shows the information of the building and its structural members. To consider the effect of crack at concrete building, effective stiffness was applied.
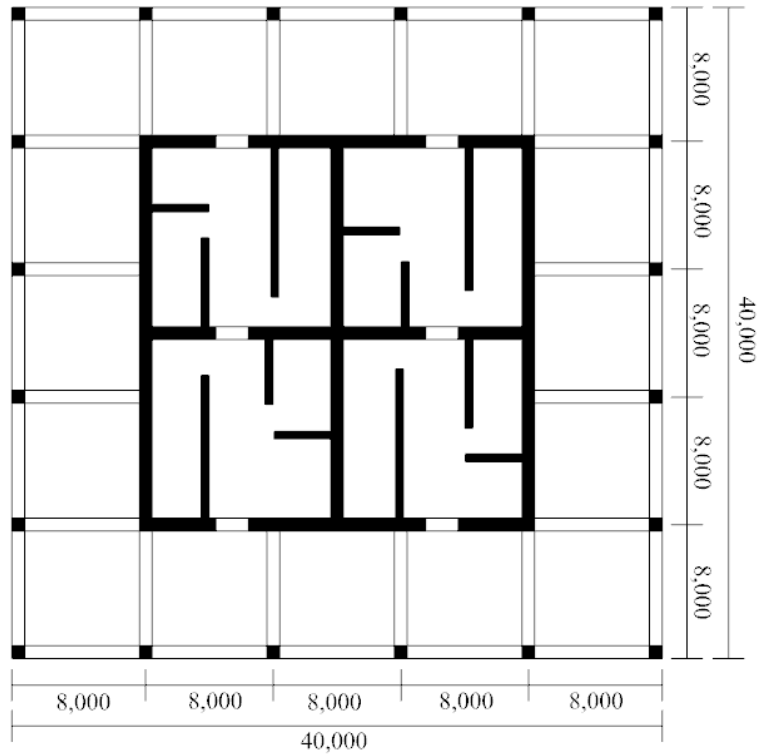
Figure 4-1 Structural plan of case study building

Table 4-1 Basic property of building

Structural system	Building frame system with core wall
Breadth (B), Depth (D), Height (H)	$B = D = 40$ m, $H = 200$ m
Story height	4 m $\times$ 50 stories
Concrete property	$f_c' = 40$ MPa, $E_c = 24.8$ GPa
Steel property	$f_y = 500$ MPa, $E_s = 200$ GPa
Damping ratio	1.2 %

Table 4-2 Structural member property

Structural member	Size		Effective stiffness
Core wall	Main core wall : 600 mm Internal wall : 300 mm		$0.7EI_g$, $1.0GA$
Column	1st~10th story	1100×1100 mm	$0.7EI_g$, $1.0GA$
	11th~20th story	1000×1000 mm	
	21st~30th story	900×900 mm	
	31st~40th story	800×800 mm	
	41st~50th story	700×700 mm	
Beam	600×800 mm		$0.3EI_g$, $1.0GA$
Slab	210 mm		Rigid diaphragm

4.1.2 Modal analysis

Figure 4-2 and **Table 4-3** show the modal shapes and natural frequency of the building. Because building has symmetric shape with square plan and core wall, clear directional mode shapes were observed.

(a) x-direction (a) y-direction
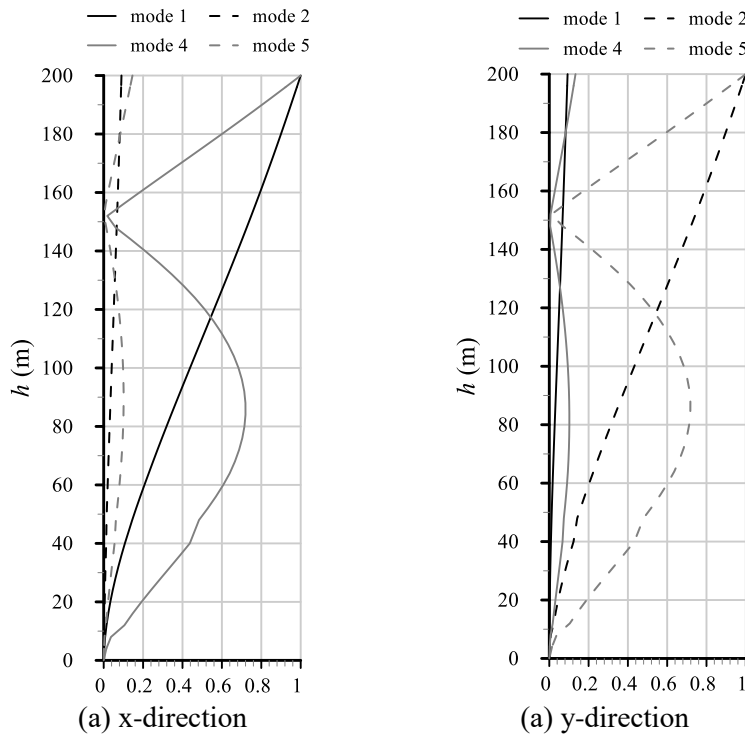
Figure 4-2 Mode shape of case study building

Table 4-3 Modal property of case study building

Mode	Period (sec)	UX	UY	RZ
1	5.03	0.992	0.008	0
2	4.96	0.008	0.992	0
3	3.12	0	0	1
4	1.32	0.981	0.019	0
5	1.28	0.019	0.981	0
6	0.94	0	0	1

4.2 Comparison of building response

Time history analysis on the case study building was conducted with the wind load data obtained from CFD and WTT.

Figure 4-3 and **4-4** shows the mean and fluctuating responses of building, respectively. Due to the difference on the assessment of wind pressure of building, structural response also showed the difference. Most of responses showed a good agreement within error of 10%, but a large error was found for some cases at along-wind standard deviation at wind angles 15° and 30°, and across-wind standard deviation at wind angle 45°.
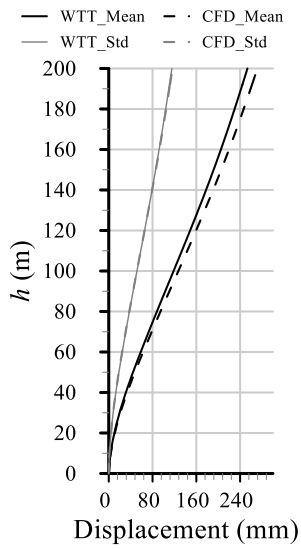
(a) Wind angle 0°, along-wind
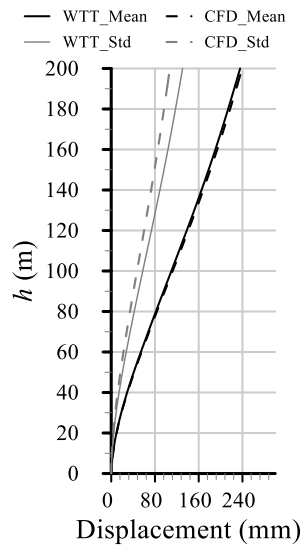
(b) Wind angle 0°, across-wind
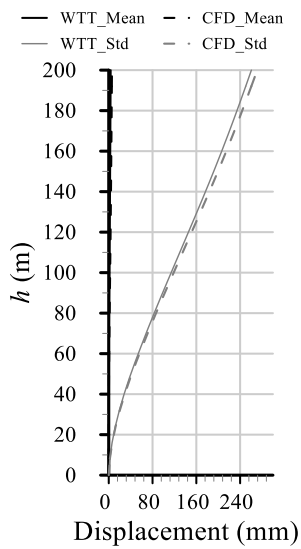
(c) Wind angle 15°, along-wind
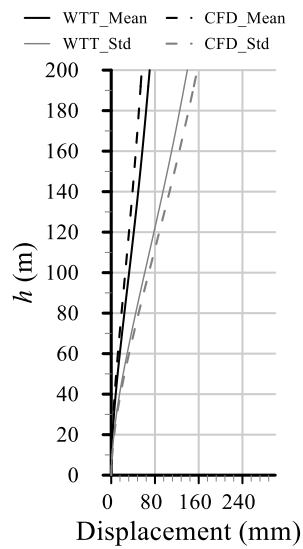
(d) Wind angle 15°, across-wind

Figure 4-3 Wind response of building – wind incident angle 0° and 15°
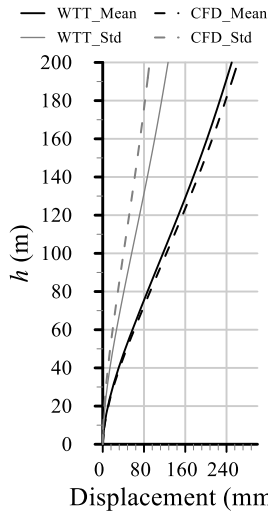
(a) Wind angle 30°, along-wind   (b) Wind angle 30°, across-wind
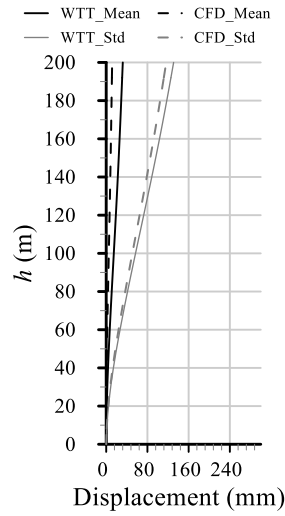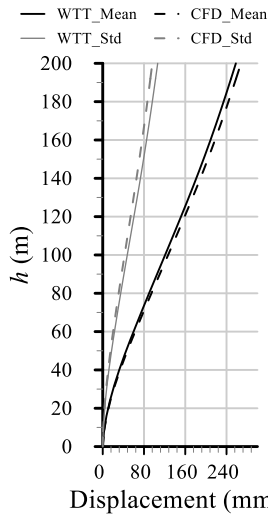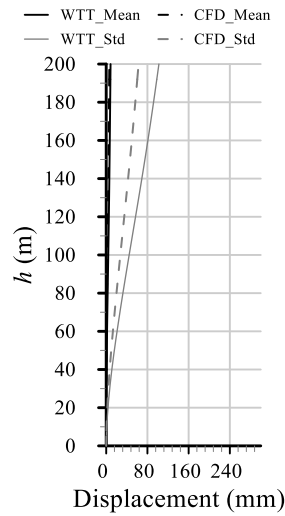
(c) Wind angle 45°, along-wind   (d) Wind angle 45°, across-wind

Figure 4-4 Wind response of building – wind incident angle 30° and 45°

4.3 Design wind load assessment

4.3.1 Peak wind load assessment with Davenport peak factor

For the assessment of design wind load from the time history data, peak response should be determined. To assess the peak of fluctuating data, peak crossing number is used to estimate how frequently the peak of data is observed. Rice (1945) showed that peak crossing number can be obtained from the power spectrum using the following equation.

$$\nu_0 = \sqrt{\frac{\int S(f)f^4 df}{\int S(f)f^2 df}}$$
(4-1)

where ν_0 is peak crossing number, S is power spectrum, and f is frequency.

Davenport (1964) suggested the peak factor of Gaussian distributed random data, which shows the ratio of standard deviation and peak fluctuation. The following equation shows the peak factor g suggested by Davenport (1964).

$$g = \sqrt{2\ln(\nu_0 T)} + \frac{0.5772}{\sqrt{2\ln(\nu_0 T)}}$$
(4-2)

where T is duration of applied wind load. With higher peak crossing number and longer duration, higher peak factor is obtained.

KDS 2022:41 follows the current theories for assessment of the design wind load. When estimating equivalent static wind load, not the peak wind load but peak wind response should be discussed for structural safety. Because resonant component plays a big role for the wind response, peak crossing number in KDS 2022:41 is estimated using the natural frequency of building. **Table 4-4** shows the peak crossing number for directional wind loads and peak factor in KDS 2022:41, which correspond to the peak of 10 minute (600 second) data. For peak factor, KDS 2022:41 uses the simplified equation of Davenport peak factor.

Table 4-4 Peak crossing number in KDS 2022:41

Wind direction	Peak crossing number	Peak factor
Along-wind	$\nu_0 = n_D \sqrt{\dfrac{R_D}{R_D + B_D}}$	$g = \sqrt{2\ln(\nu_0 T) + 1.2}$
Across-wind	$\nu_0 = n_L$	$g = \sqrt{2\ln(\nu_0 T) + 1.2}$
Torsional	$\nu_0 = n_T$	$g = \sqrt{2\ln(\nu_0 T) + 1.2}$

Figure 4-5 shows the power spectrum of top floor displacement response at wind incident angle 0. As shown in the power spectrum, resonant component shows high contribution. While PSD of wind load for along-wind did not shows a local peak and across-wind showed a peak at Strouhal number of 0.1, both PSDs of along- and across-wind responses showed a peak at building's natural frequency.

Table 4-5 shows the peak factor obtained from the top floor displacement. Due to the high contribution of resonant component, most of the peak factors showed good agreement with WTT and CFD, as well as the peak factor specified in KDS code.

(a) Along-wind   (b) Across-wind
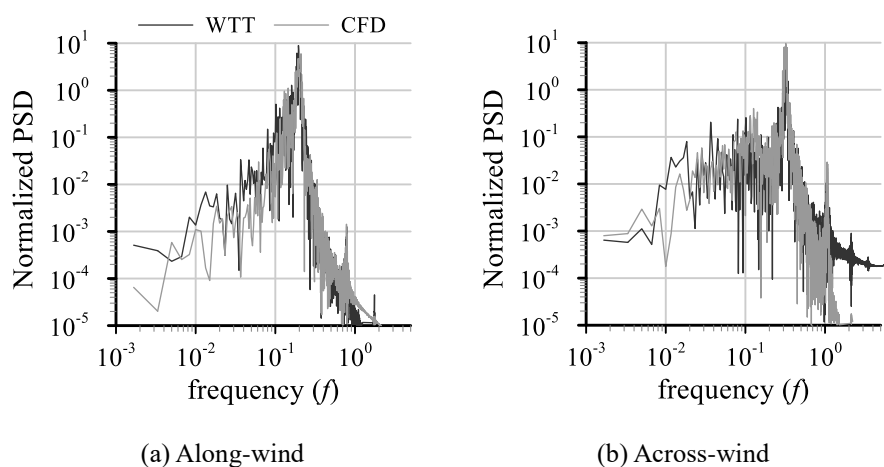
Figure 4-5 PSD of directional response at top floor

Table 4-5 Peak factor by Davenport method

Direction	KDS	Angle	0°	15°	30°	45°
Along-wind	3.24	WTT	3.23	3.26	3.26	3.23
		CFD	3.27	3.26	3.28	3.23
Across-wind	3.29	WTT	3.27	3.26	3.28	3.28
		CFD	3.27	3.28	3.28	3.27
Torsional-wind	3.42	WTT	3.41	3.41	3.39	3.40
		CFD	3.40	3.42	3.40	3.40

4.3.2 Non-Gaussian distribution peak

Limitation of the Davenport peak factor is that Davenport peak factor is based on the Gaussian distribution. For non-Gaussian distribution, peak value becomes different even though the peak crossing number is same. If fluctuating function follows the Gaussian distribution, its skewness and kurtosis should become 0 and 3, respectively. **Figure 4-8** shows the probability distribution of the top floor displacement response at wind incident angle 0. As shown in the figure and its skewness and kurtosis, wind response does not follow the Gaussian distribution.

(a) Along-wind

(skewness = 0.04, kurtosis = 2.21)

(b) Across-wind

(skewness = 0.03, kurtosis = 4.41)
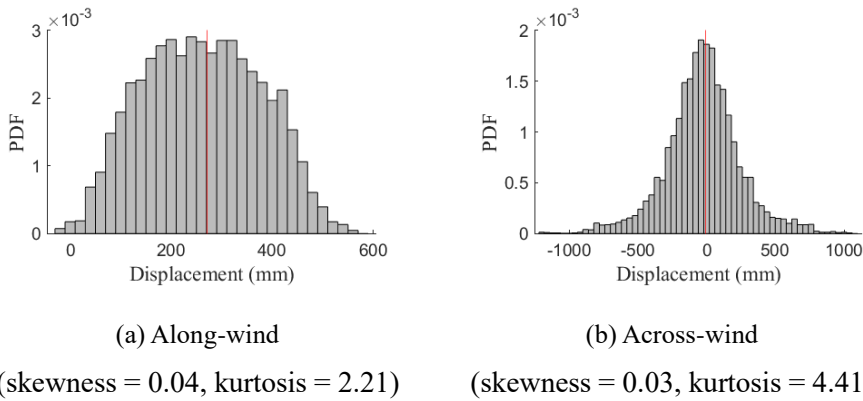
Figure 4-6 Probability density function of directional response

For evaluating the peak of non-Gaussian distribution, two of the most popular methods are Gumbel-fitting method and translation method. Based on the assumption that natural wind follows the Gumbel distribution, Gumbel-fitting method fits the non-Gaussian data to Gumbel distribution. The translation method uses a translation function to fit the non-Gaussian data to the Gaussian distribution. **Figure 4-7** shows the brief procedure of evaluating the non-Gaussian peak factor summarized by Peng *et al.* (2014).

Peng *et al.* (2014) suggested two translation methods and compared the existing methods and suggested methods to evaluate the peak value of non-Gaussian distribution, and claimed that Gumbel-fitting and translation methods with Hermite polynomial model (HPM) show the consistent performance for peak value estimation. While Gumbel-fitting method requires

a long duration of data for division into segments, translation method can be applied for any length of data. Due to the short length of CFD simulation, HPM translation method is used for the peak value evaluation of non-Gaussian distribution in this study.

```
┌─────────────────┐   ┌─────────────────┐   ┌─────────────────┐
│ Measured record x│→ │ Truncate x into N│→ │Take the peak from each│
│ of length t_total│   │segments of length t│   │ segment x_p1, ..., x_pN│
└─────────────────┘   └─────────────────┘   └─────────────────┘

┌─────────────────┐   ┌─────────────────┐   ┌─────────────────┐
│Gumbel distribution of│← │ Convert U_t, α_t │← │Estimate parameters U_t, α_t│
│peak for longer duration T│   │ to U_T, α_T │   │ of Gumbel distribution│
└─────────────────┘   └─────────────────┘   └─────────────────┘
```

(a) Gumbel-fitting method

```
                    ┌──────────────────────────┐
                    │ Translation function x=g(u)│
                    │ u follows Gaussian distribution│
┌─────────────┐     └──────────────────────────┘     ┌─────────────┐
│Measured record│→                                    → │Peak distribution│
│ x of length t │     ┌─────────────┐ ┌─────────────┐   │    of x     │
└─────────────┘   → │Peak crossing│→│Peak distribution│→ └─────────────┘
                    │ number υ    │ │   of u      │
                    └─────────────┘ └─────────────┘
```

(b) Translation method

Figure 4-7 Procedure for non-Gaussian peak evaluation
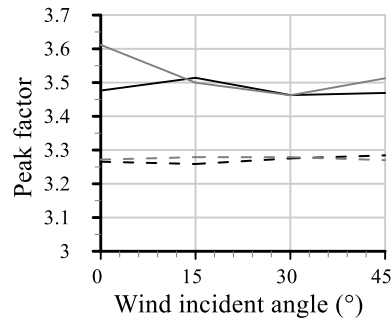
Figure 4-8 compares the peak factors obtained using Davenport method and HPM translation method. Peak factor increased about 0.2 for across- and torsional-wind for both WTT and CFD. For along-wind direction, only the result by CFD showed a peak factor drop of 0.1 and WTT did not show a clear difference with Davenport peak factor.
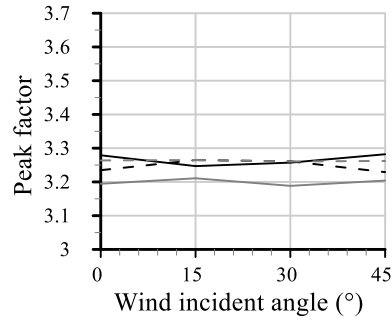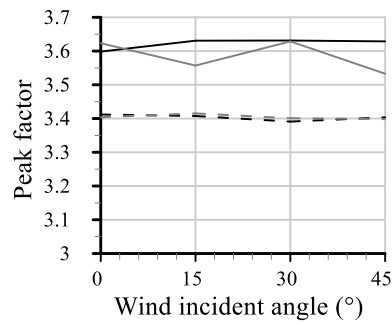
Figure 4-8 Peak factor for non-Gaussian distribution

Figures 4-9 and 4-10 show the peak wind load with consideration of non-Gaussian peak factor. While along- and across-wind loads showed sufficient accuracy within an error of 20% for CFD, high underestimation of CFD was found in the torsional-wind load. For across-wind load, profile of CFD and WTT showed some difference in the location of peak wind load. While WTT shows a peak wind load at a height of 140 m, CFD shows a peak wind load at height of 100 m, which results in the lower base overturning moment even though the shear force is similar.

Figure 4-11 shows the peak base overturning moment evaluated by wind tunnel test and CFD. For both methods, tendency of the base overturning with respect to wind incident angle showed good agreement. Figure 4-12 shows the error percentage of the base overturning moment conducted by CFD compared to the wind tunnel test. For along- and across-wind loads, CFD fits with the wind tunnel test within an error of 15%. For torsional-wind load, CFD showed a large underestimation of wind load with error up to 60%. For current methods, CFD can be applicable to the determination of along- and across-wind loads, but development on the accuracy of torsional wind load is required.
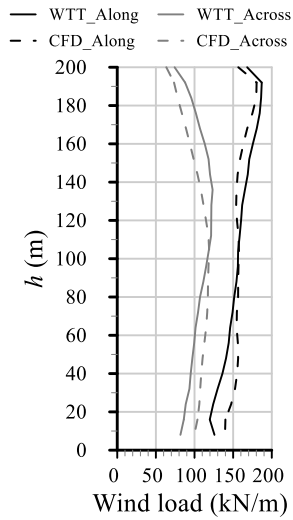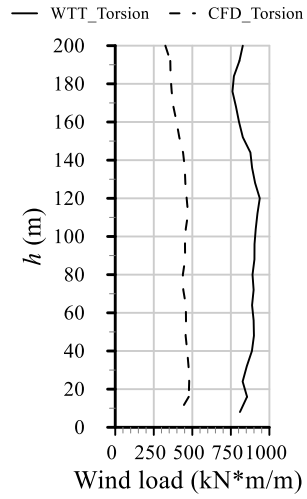
(a) Wind angle 0°, along-wind   (b) Wind angle 0°, across-wind
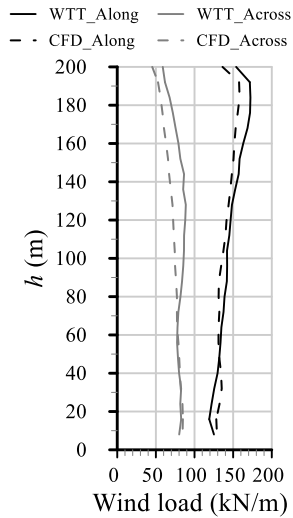
(a) Wind angle 0°, along-wind   (b) Wind angle 15°, across-wind

Figure 4-9 Peak wind load with height for wind incident angle 0° and 15°

(a) Wind angle 30°, along-wind (b) Wind angle 30°, across-wind
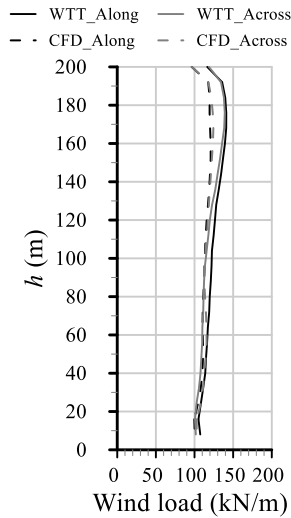
(c) Wind angle 45°, along-wind (d) Wind angle 45°, across-wind

Figure 4-10 Peak wind load with height for wind incident angle 30° and 45°

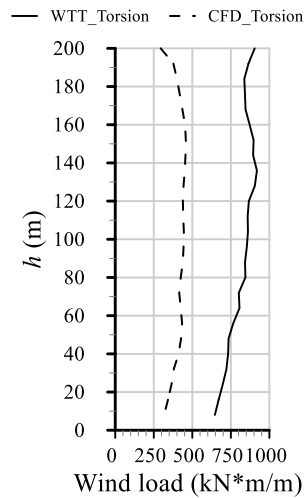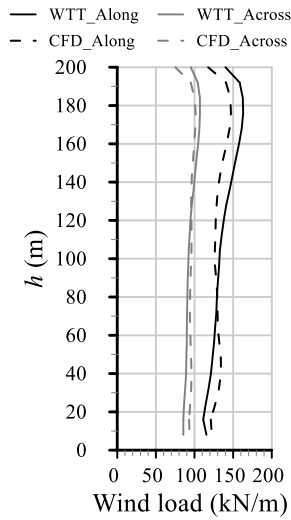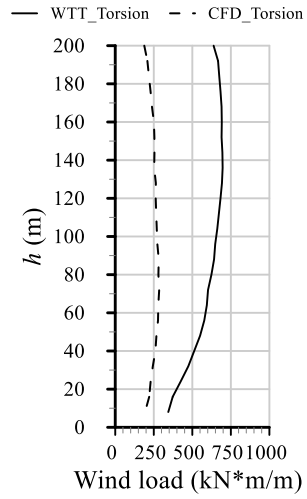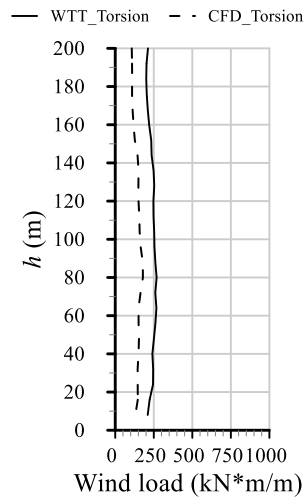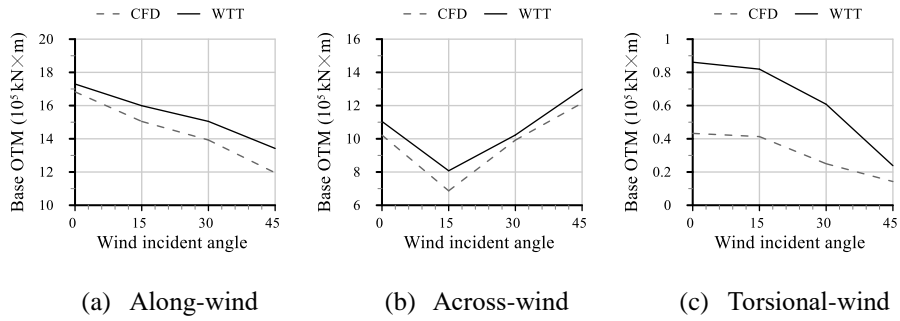(a) Along-wind (b) Across-wind (c) Torsional-wind

Figure 4-11 Peak base overturning moment

(a) Along- and Across-wind (b) Torsional-wind
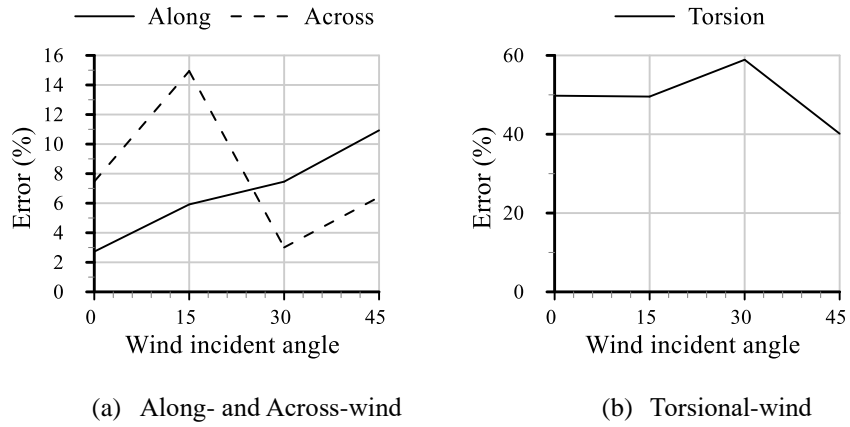
Figure 4-12 Error percentage of evaluated peak O.T.M.

4.4 Discussion

In this chapter, time history analysis is conducted to assess the peak wind response and wind load.

Wind responses based on CFD and WTT showed a good agreement within 10% error except for some cases with high errors. From the response, peak factor and corresponding peak wind load was evaluated. Peak wind load showed a good agreement for along- and across-wind loads with error up to 20%, but significant underestimation of torsional-wind load up to 60% was observed. Due to the effect of high torsional moment at the corner with unusual pressure by vortex shedding, CFD is yet inaccurate for evaluating torsional wind load.

Davenport peak factor obtained by CFD showed good agreement with WTT due to the good agreement of PSD of wind load by high contribution of resonant component. When non-Gaussian distribution is considered in the peak factor, peak factor increased for across- and torsional wind response. For along-wind load, peak factor decreased only for CFD simulation while WTT did not show clear difference. From the difference between non-Gaussian peak factor and Davenport peak factor, estimated peak wind load can show up to 8% difference. Reason of non-Gaussian peak comes from not only the distribution of wind load but also the structural property, so method to predict the non-Gaussian effect should be discussed in further study.

Chapter 5. Effect of Pressure Tap on Wind Load Assessment

To obtain the force and overturning moment of wind on the building by CFD simulation or HFPI test, wind pressure should be integrated with its tributary area. Because HFPI test requires integration to obtain the wind force and moment on the building, accuracy of the HFPI test in structural design is dependent on the resolution of pressure taps. There were several previous studies on the comparison of HFPI and HFFB wind tunnel test (Cluni *et al.*, 2011, Kim *et al.*, 2010). Limited number of the pressure taps in HFPI test can occur the error on the integrated wind load and base overturning moment.

Compared to the wind tunnel test, CFD has strength with unlimited number of pressure taps, which has advantage in integrating wind pressure. However, remaining problem of CFD is its computational cost. Even though Chapters 3 and 4 showed that CFD can evaluate the responsible wind load and response, ensemble averaging analysis was not conducted which remains the uncertainty problem. To overcome such an issue, combined usage of CFD and WTT is discussed.

This chapter first analyzes the characteristic of integrating wind load in terms of correlation and power spectrum. Then, comparison of the integrated wind load with the different number and locations of wind pressure taps is conducted. Analysis was done for both CFD and WTT result with the same pressure tap distribution cases. Then, the difference between the cases for both CFD and WTT was evaluated to verify if CFD can be used for adjusting the result of WTT.

5.1 Characteristic of integrated wind load

Before comparing the effect of leakage of wind pressure tap on the wind load assessment, characteristic of integrated wind load is discussed to check if CFD shows similar scheme with wind tunnel test.

5.1.1 Correlation between floor load

While PSD of the wind pressure usually follows the spectral property of the incident wind, PSD of the integrated load follows the aerodynamic characteristic of a building due to the correlation between the wind pressure at each location. Because of it, PSD of the integrated wind load is affected by the number of pressure taps.

Figures 5-1 to 5-3 show the correlation between directional wind load on each floor with wind load at height $h = 0.25H$, $0.5H$, and $0.75H$. Correlation showed good agreement of CFD and WTT for across-wind, but small correlation between height loads was found for along- and torsional-wind load. For both cases, CFD showed lower correlation than WTT. While correlation between top and bottom showed correlation larger than 0.3 for WTT, correlation for CFD dropped to 0.
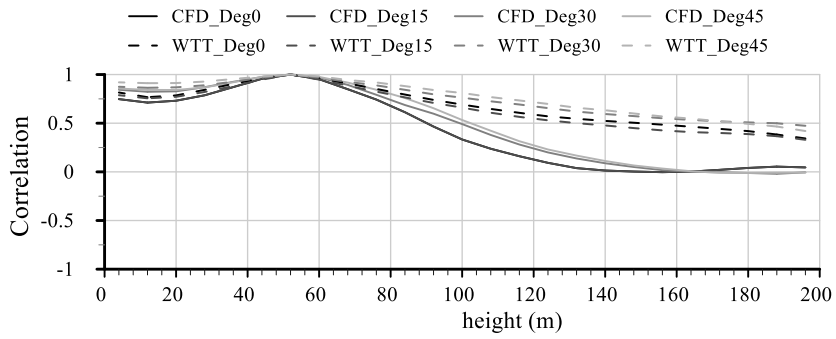
(a) Correlation with height $h = 0.25H$
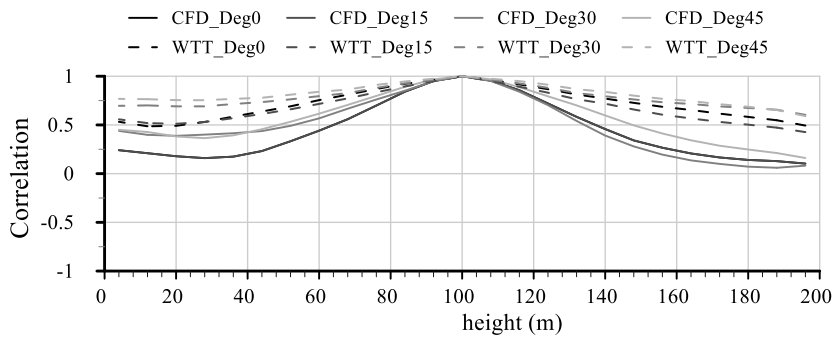
(b) Correlation with height $h = 0.5H$
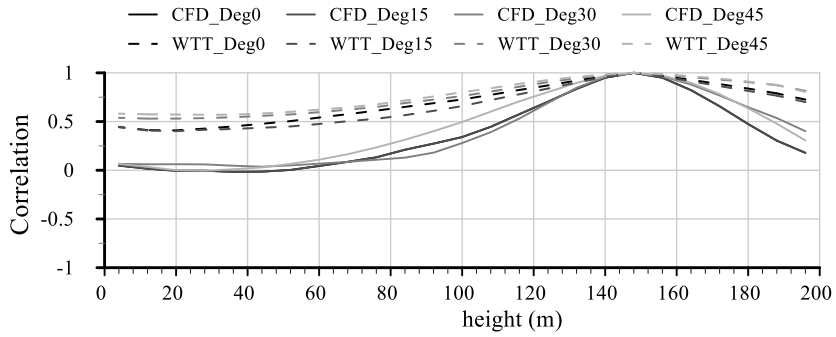
(c) Correlation with height $h = 0.75H$

Figure 5-1 Correlation of wind loads with height – along-wind

68

(a) Correlation with height $h = 0.25H$

(b) Correlation with height $h = 0.5H$

(c) Correlation with height $h = 0.75H$

Figure 5-2   Correlation of wind loads with height – across-wind

69

(a) Correlation with height $h = 0.25H$

(b) Correlation with height $h = 0.5H$

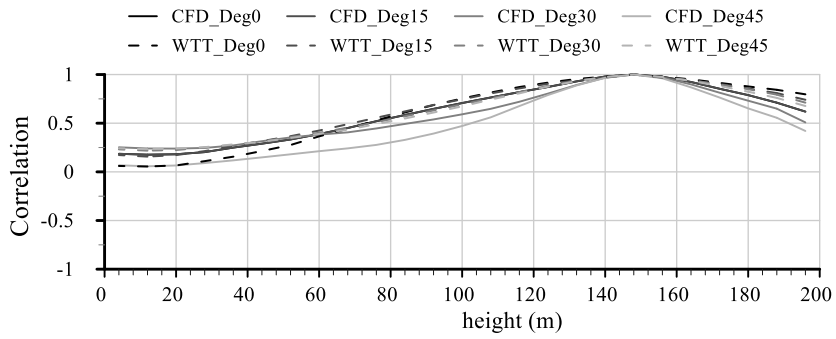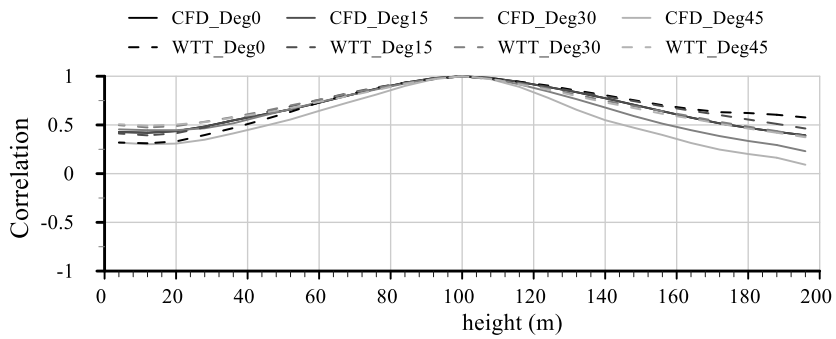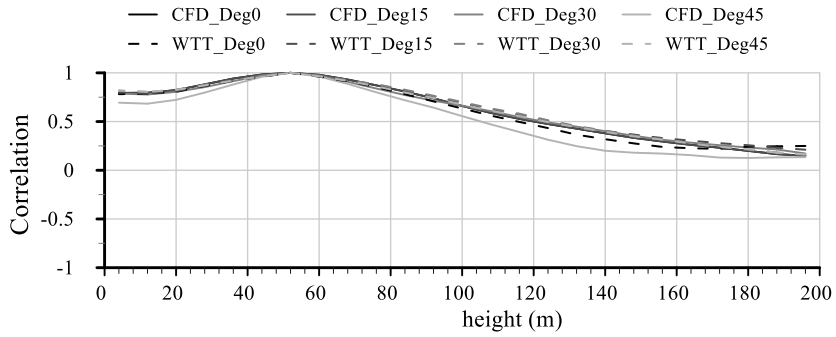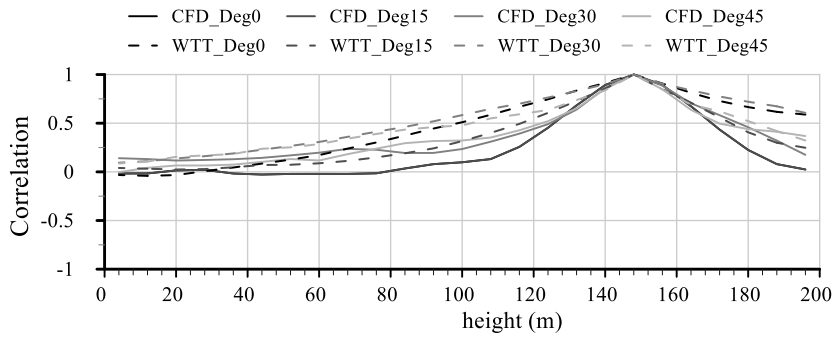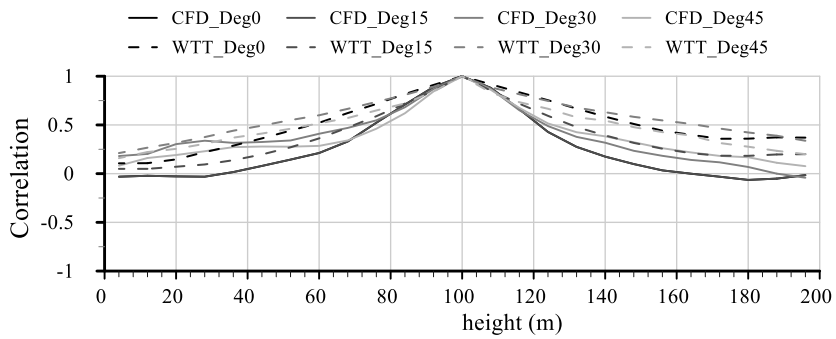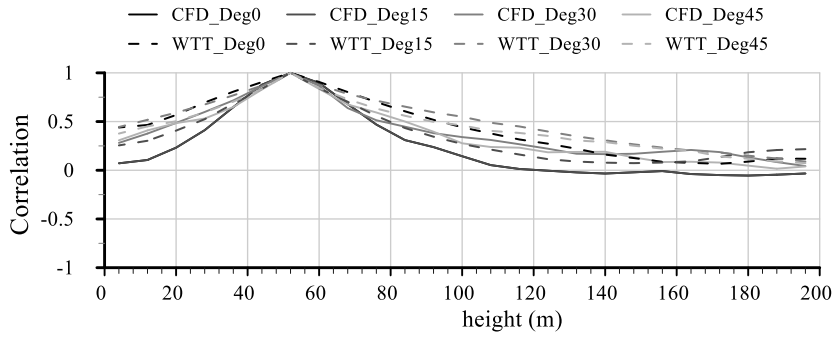(c) Correlation with height $h = 0.75H$

Figure 5-3 Correlation of wind loads with height – torsional-wind

70

5.1.2 Spectral characteristic of wind pressure integration

Coherence function is commonly used to analyze the correlation between the discrete data in the frequency domain, but coherence can be only used to compare two discrete data and hard to summarize the total fluctuating field. To discuss the spectral characteristic of wind pressure integration, total wind pressure field needs to be discussed simultaneously. Let the energy of fluctuating wind pressure or wind load on each floor is directly integrated without considering correlation. Then, its magnitude is higher than the energy of fluctuating base overturning moment due to the phase difference of the fluctuating pressure between the pressure taps.

To compare the directly integrated energy of wind pressure and floor load, integrated PSD of wind pressure and floor load S_{PT} and S_{FT} is defined as following function.

$$S_{PT}(f) = \int S_p(f) dA_p \qquad (5\text{-}1)$$

$$S_{FT}(f) = \int S_f(f) dh_f \qquad (5\text{-}2)$$

S_p and S_f is PSD of wind pressure and wind load on pressure tap and story, A_p and h_f is tributary area of pressure tap and height of story.

Figure 5-4 shows the integrated PSD of wind pressure, floor load and PSD of base overturning moment from the WTT and CFD with wind incident angle 0°. In this plot, each PSD was not normalized to compare the size of integrated energy. **Figure 5-5** shows the ratio between the PSD of base overturning moment and integrated PSD of wind pressure and floor load which can be expressed as follows:

$$R_i(f) = \frac{S_i(f)}{S(f)} \qquad (5\text{-}3)$$

where S is PSD of base overturning moment, S_i is S_p or S_f, and R_i is PSD ratio between integrated PSD and PSD of base overturning moment.
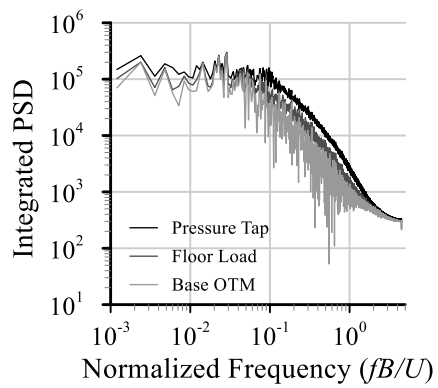
71

Frequency of PSD function of wind load represents the size of eddy, which gets smaller as frequency increase. For the high frequency region, fluctuation of the wind pressures at different locations of the building loss its correlation. Thus, the PSD ratio of **Figure 5-5** tends to get higher as frequency gets higher because the energy of fluctuating wind pressure is dissipated at the integrated load. For the across-wind load, PSD ratio gets minimum value at the normalized frequency of Strouhal number. This is because of the vortex shedding at the corner or building which simultaneously affects the wind pressure at sidewalls. For torsional-wind load, PSD ratio for integrated PSD of wind pressure also showed high value for low frequency region. This is because the method of integrating PSD do not consider the direction of torsion which can get the inverse value with pressure tap's location. Because the torsional-wind load is affected by both along- and across-wind load, it did not show uniform tendency with the frequency, but local peak was found at normalized frequency with Strouhal number.

Comparing WTT and CFD, PSD ratio by CFD showed similar tendency with WTT. PSD ratio of CFD showed higher instability than WTT because of lack of ensemble and lack of convergence in simulation. For WTT, PSD ratio showed decrement after normalized frequency 1. This might be the reason of sampling noise of HFPI test, which was also found in DMD analysis in Chapter 3. For CFD, PSD ratio also showed decrement at high frequency region. Reason of decrement is expected to be the effect of method of LES, which assumes the effect of eddies smaller than the mesh size using the filter.
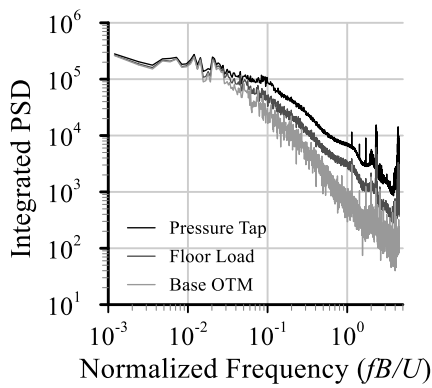
(a) Along-wind, WTT

(d) Along-wind, CFD

(b) Across-wind, WTT

(e) Across-wind, CFD

(c) Torsional, WTT

(f) Torsional, CFD

Figure 5-4 PSD of base overtuning moment and integration of PSD of nodal pressure and floor load with wind incident angle 0°
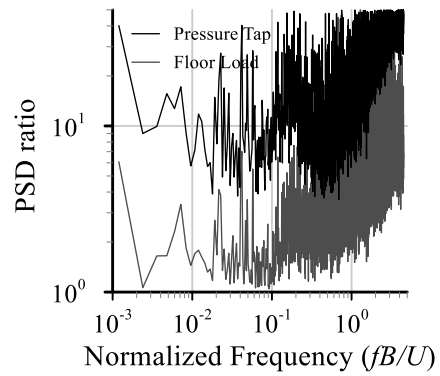
Figure 5-5 PSD ratio of base overturning moment PSD and integrated PSD of nodal pressure and floor load

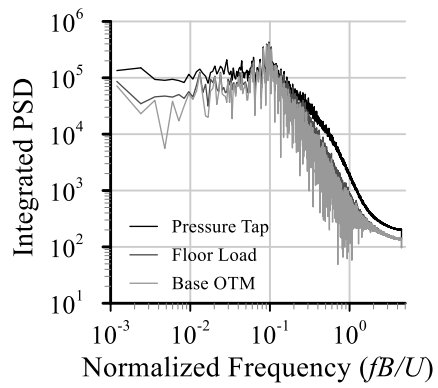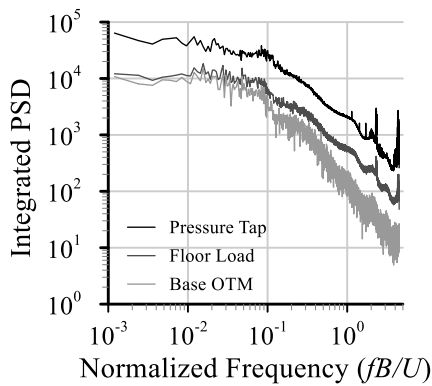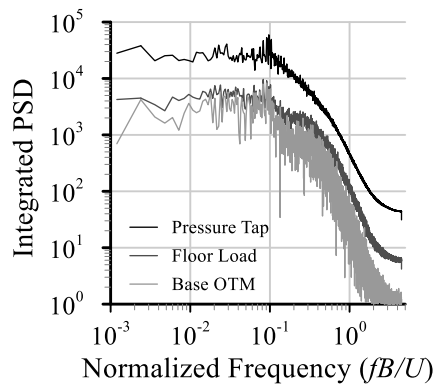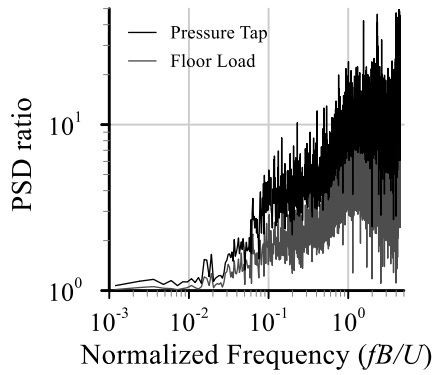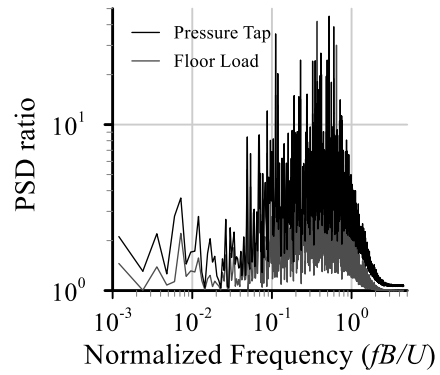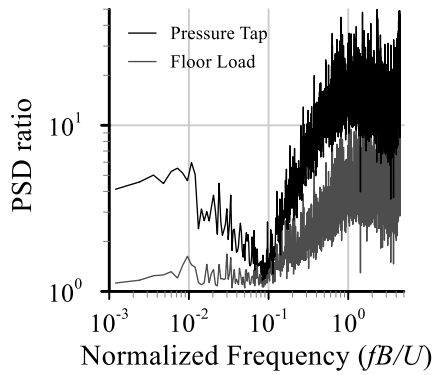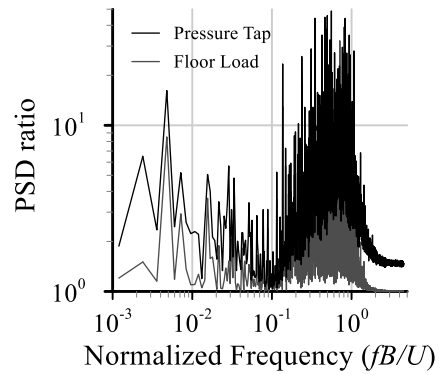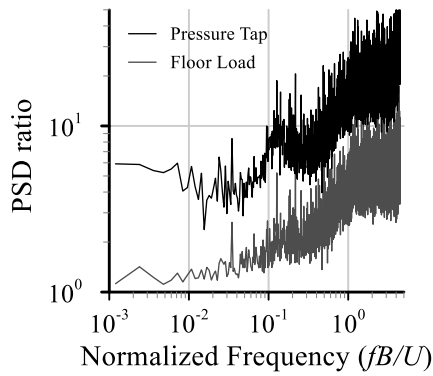While **Figures 5-4** and **5-5** are about wind load with wind incident angle 0°, same analysis can be applied to other wind incident angles. For integration of PSD of pressure taps, every taps on building should be integrated for both along- and across-wind load. Instead, x-direction and y-directional wind load on building where the x and y direction belongs to building's axis can be discussed. When wind incident angle is 0°, x-dir. and y-dir. will be equal to along- and across-wind direction.

Similar to PSD ratio of along- and across-wind load, logarithm of x-dir. and y-dir. PSD ratio also shows linear trend with division at the normalized frequency with Strouhal number. **Figure 5-6** and **5-7** shows the linear regression of logarithm of x-dir. and y-dir. PSD ratio for WTT data with various wind incident angles. Because the PSD ratio lost its tendency after the normalized frequency 1, PSD ratio for lower frequency was used for regression. For wind incident angle 45°, PSD ratio of x-dir. and y-dir. shows similar tendency due to the symmetricity.

Linear regression for every CFD data and every wind incident angle cases from TPU aerodynamic database with 0° to 50° was obtained. **Figure 5-8** shows the coefficient of linear regressions for logarithm of PSD ratio for both CFD and WTT. For this figure, wind angle represents the angle between the wind and building's direction of façade. For example, when wind incident angle is 0°, wind angle of x-dir. will be 0° and y-dir. will be 90°. As shown in the result, every coefficient of linear regression from WTT shows clear tendency with façade angle. For linear regression from CFD, coefficients with wind angle showed similar tendency with WTT, but most of coefficients showed the error.
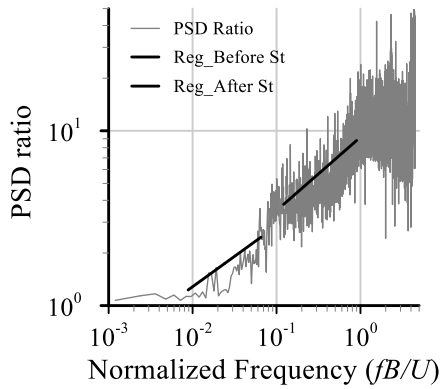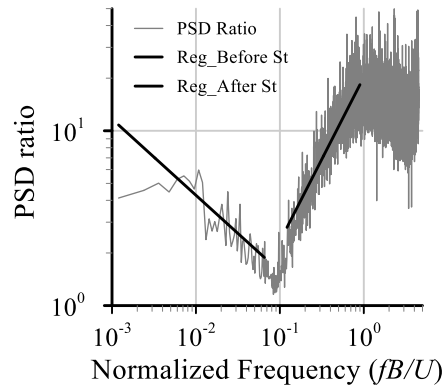
(a) X-Dir, Wind incident angle 0°   (b) Y-Dir, Wind incident angle 0°
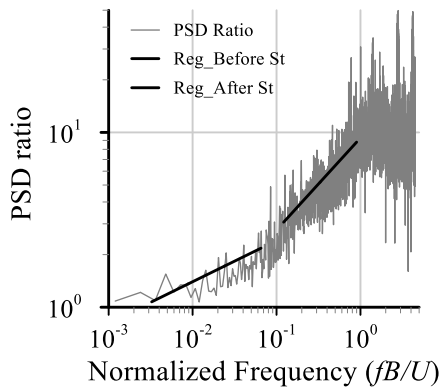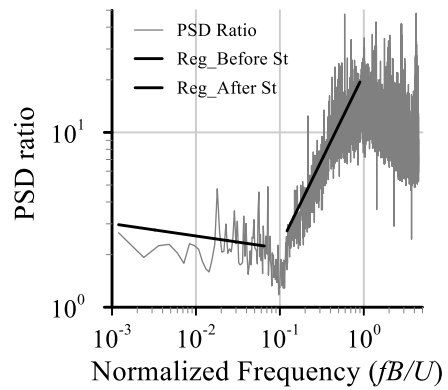
(c) X-Dir, Wind incident angle 15°   (d) Y-Dir, Wind incident angle 15°

Figure 5-6 Linear regression of PSD ratio with wind incident angle 0° and 15°
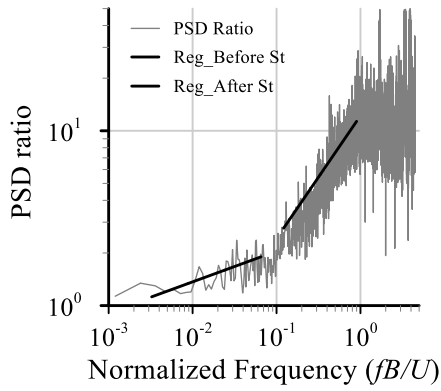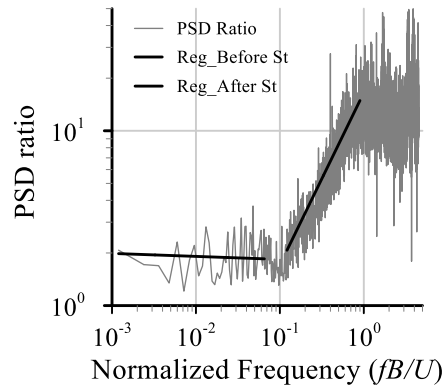
(a) X-Dir, Wind incident angle 30　　　(b) Y-Dir, Wind incident angle 30
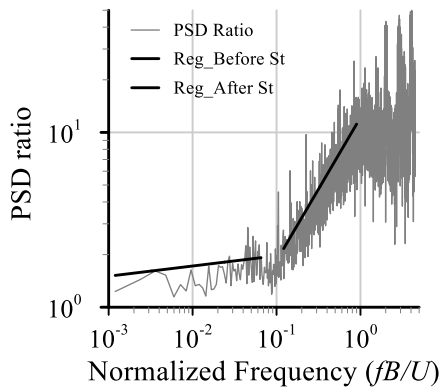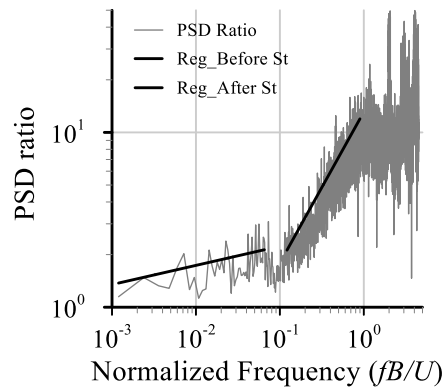
(c) X-Dir, Wind incident angle 45　　　(d) Y-Dir, Wind incident angle 45

Figure 5-7 Linear regression of PSD ratio with wind incident angle 30° and 45°
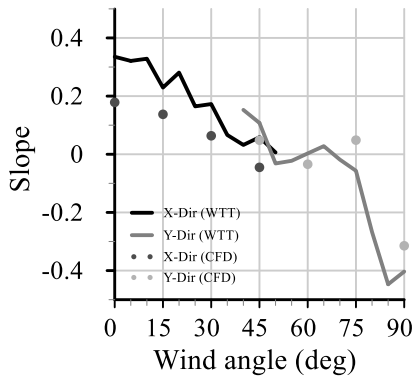
(a) Gradient, Before Strouhal number   (b) Constant, Before Strouhal number
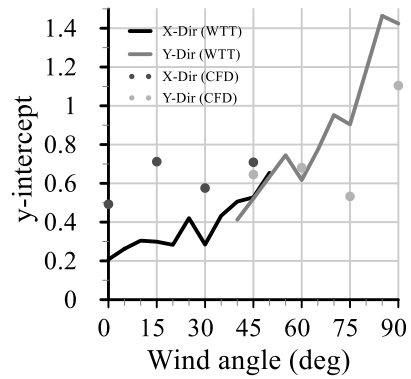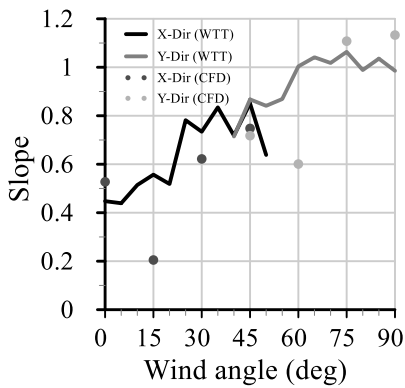
(c) Gradient, After Strouhal number   (d) Constant, After Strouhal number
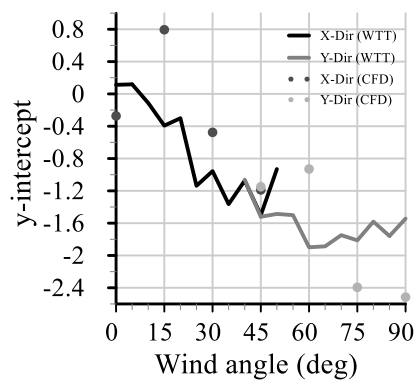
Figure 5-8 Coefficient of linear regression of PSD ratio

5.2 Integrated wind load with various pressure tap selection

5.2.1 Pressure tap selection

Commonly, it is quite rare to use 125 pressure taps in a single façade of building in HFPI test due to the high cost of equipment. Park and Yeo (2021) compared the effect of pressure tap distributions of HFPI test. Park and Yeo denoted that horizontal pressure tap resolution effects more critical than the vertical tap resolution.

With assumption of limited number of wind pressure tap, two cases of horizontal and five cases of vertical tap selections was defined based on the other researches of HFPI tests. **Table 5-1** shows the selected horizontal and vertical location of pressure taps of each cases with selecting every pressure taps in single height. For vertical cases, case A shows the original data with every 25 heights selected. Case B and C is case with 9 heights selected, and case D and E is case with 7 heights selected. While case B and D have uniform vertical distance between the pressure taps, case C and E have concentrated distribution of pressure tap at higher height of building where the wind pressure have higher influence on the base overturning moment and building response.

Table 5-1 Pressure tap selections for limited number of pressure tap

Horizontal	1	$0.1B, 0.3B, 0.5B, 0.7B, 0.9B$
	2	$0.1B, 0.5B, 0.9B$
	3	$0.2B, 0.4B$
Vertical	A	Every 25 heights $(0.02H \sim 0.98H)$
	B	$h = 0.02, 0.14, 0.26, 0.38, 0.50, 0.62, 0.74, 0.86, 0.98\ H$
	C	$h = 0.18, 0.34, 0.50, 0.62, 0.70, 0.78, 0.86, 0.94, 0.98\ H$
	D	$h = 0.02, 0.18, 0.34, 0.50, 0.66, 0.82, 0.98\ H$
	E	$h = 0.18, 0.38, 0.58, 0.70, 0.82, 0.94, 0.98\ H$

5.2.2 Error on the integrated base overturning moment

Based on the selected pressure tap location, wind load is integrated and its structural response and corresponding peak was obtained with same procedure of Chapter 4. From the results, error percentage was evaluated compared to the case 1-A which every pressure taps are selected.

Tables 5-2 and 5-3 show the average error percentage of peak wind load by WTT and CFD considering 4 wind directions. As denoted by Park and Yeo (2021), horizontal tap distribution showed a larger effect than vertical tap distribution. For vertical tap distribution, usually wind pressure tap is concentrated in the higher height for evaluation of peak wind pressure, but case D and E showed a higher error than case B and C in terms of integrated wind load.

Figures 5-9 and 5-10 show the scatter plot of WTT and CFD for error on the mean, standard, and peak base overturning moment. Considering that square section building have relatively small mean across- and torsional-wind load, only along-wind load was compared for the mean base overturning moment in **Figure 5-9**. For most cases, two method showed positive correlation on the error. Linear graphs show the linear regression of scattered errors. CFD showed about 133% error of WTT. Colored region shows the region with error by CFD shows same sign with WTT and lower than twice of WTT, where the reduction of error by revising using CFD is expected. For case 1 and 2 of horizontal tap selection, most of the cases showed that CFD can reduce the error. For case 3, along-wind load still showed good agreement of CFD and WTT, but negative effect was observed for the across- and torsional-wind directions.

Table 5-2 Average error (%) of peak wind load occurred by WTT

	Case	A	B	C	D	E
Along-wind	1	0.00	1.33	0.03	1.89	0.16
	2	2.13	3.40	2.16	3.83	2.11
	3	4.91	3.43	4.87	2.64	4.82
Across-wind	1	0.00	1.20	0.14	2.13	0.41
	2	1.92	2.76	1.89	3.57	2.23
	3	6.38	4.79	6.35	3.71	6.00
Torsional-wind	1	0.00	0.74	4.13	0.74	4.56
	2	7.03	7.05	7.22	5.89	7.27
	3	29.66	29.06	26.07	28.88	25.11

Table 5-3 Average error (%) of peak wind load occurred by CFD

	Case	A	B	C	D	E
Along-wind	1	0.00	1.64	0.10	2.70	0.27
	2	2.62	4.17	2.68	5.19	2.86
	3	5.89	4.23	5.77	3.61	5.56
Across-wind	1	0.00	1.21	0.18	1.98	0.62
	2	1.59	2.64	1.69	3.41	2.03
	3	4.57	3.84	4.47	3.83	4.37
Torsional-wind	1	0.00	1.54	3.55	2.03	4.48
	2	2.47	1.90	6.25	2.48	6.81
	3	40.69	40.48	38.42	40.75	36.51
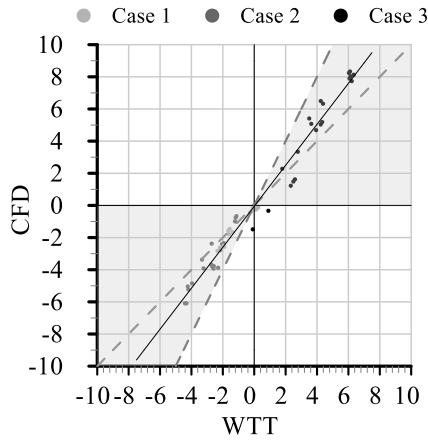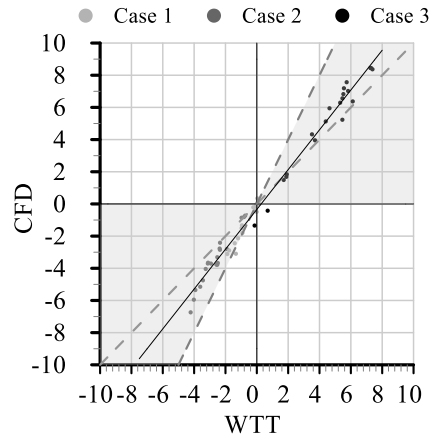
(a) Mean error – Along-wind   (b) Fluctuating error – Along-wind
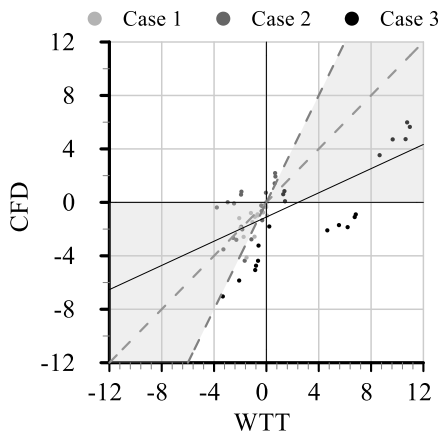
(c) Fluctuating error – Across-wind   (d) Fluctuating error– Torsional-wind

Figure 5-9 Scatter plot of error on the mean and fluctuating base overturning moment
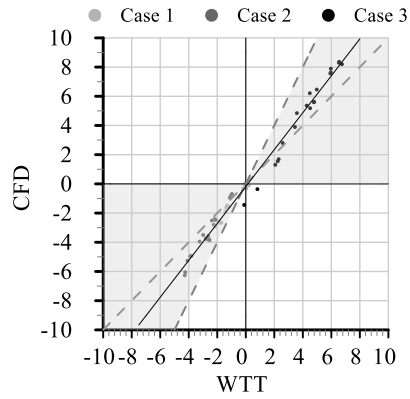
(a) Mean error – Along-wind
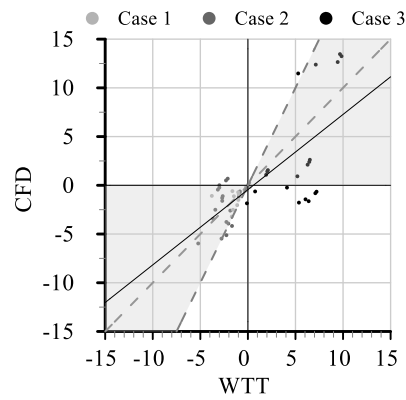
(b) Mean error – Across-wind
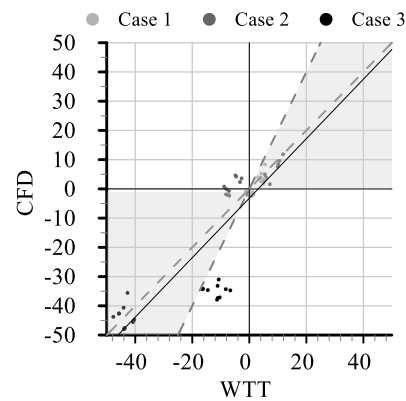
(c) Mean error – Torsional-wind

Figure 5-10 Scatter plot of error on the peak base overturning moment

5.3 Discussion

In this chapter, effect of wind pressure integration on the assessment of wind load was discussed.

(a) Spectral property of directly integrated PSD of wind pressure and PSD of base overturning moment was discussed. Ratio between two PSDs showed the clear effect of eddy size in along-wind load and vortex shedding in across-wind load. Due to the combined effect of eddy size and vortex shedding, ratio for torsional-wind showed a complicated formula with local peak.

From the PSD ratio, linear regression was done for the along- and across-wind direction. Slope and y-intercept showed a clear tendency with respect to wind incident angle. CFD and WTT showed similar tendencies, but specific values showed consistent error.

(b) Effect of the pressure tap locations on the wind pressure integration test was conducted. Error percentage for CFD and WTT showed a high correlation with positive slope of linear regression. Most of the cases reduce the error when CFD is applied to revise the result by WTT, but some cases with negative effect were observed.

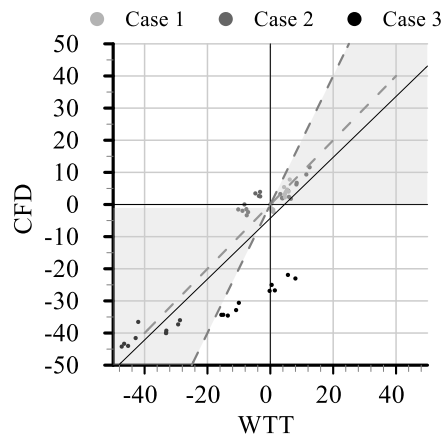Through the analysis, it can be concluded that CFD shows a good agreement with spatial characteristic obtained from WTT. By integration of CFD and WTT, it is expected to overcome the pressure tap resolution problem of WTT and high-computational cost problem for ensemble data of CFD. In further study, not only revising the error of peak wind load but also reconstructing the pressure data of WTT without the pressure tap using CFD result could be discussed.

Chapter 6. Conclusion

In this study, CFD was used to evaluate the wind load and response on the square sectioned building with comparison with the wind tunnel test. For application of CFD in the wind design, three main terms were discussed, which were the evaluation of the wind load, wind response, and application of CFD to modifying WTT result. The conclusions are listed below.

1) CFD can be used to obtain the mean and fluctuating wind pressure field on the building with some error compared to wind tunnel test. However, large error on the skewness and kurtosis of wind pressure was found. In integrated base overturning moment, CFD tends to underestimate the wind load compared to the wind tunnel test.

2) Spectral characteristic of the wind load by CFD showed a good agreement with wind tunnel test. Because of limitation of LES on the small eddy, power spectrum of the high-frequency region was underestimated in CFD. Modal analysis of wind pressure field showed a similar modes for CFD and wind tunnel test, but the order of modes showed some difference.

3) Traditional peak estimating method using Davenport peak factor and peak factor estimation of non-Gaussian distribution showed different results. Davenport peak factor followed the estimation in design code, but non-Gaussian considered peak factor showed some difference.

4) Characteristic of wind pressure on its integration to the force and moments was discussed. Energy spectrum of total fluctuating wind pressure decreases as wind pressure is integrated into loads. CFD could capture the same phenomena with wind tunnel test, but the coefficients had some difference. There is potential of CFD to use it as a tool of adjusting the HFPI wind tunnel test result with its lack of number of pressure taps.

5) Effect of the pressure tap resolution on the HFPI test and CFD was compared. Result showed that CFD shows a good agreement on the tendency of integration error and showed the potential of CFD as revising tool of HFPI test. However, some cases showed negative effect which shows larger error when CFD is applied. Further analysis on the comparison of characteristic of HFPI and CFD and the CFD simulation with higher accuracy should be done to overcome such a problem.

References

1. AIJ guidelines for practical applications of CFD to pedestrian wind environment around buildings

2. Ansys (2009), *Fluent 12 Users guide*, Fluent Inc., Lebanon.

3. Clannachan, G. H., Lim, J. B. P., Bicanic, N., Taylor, I., & Scanlon, T. J. (2009). Practical Application of CFD for Wind Loading on Tall Buildings. (January), 767–776.

4. Cluni, F., Gusella, V., Spence, S.M.J., and Bartoli, G. (2011), "Wind action on regular and irregular tall buildings: Higher order moment statistical analysis by HFFB and SMPSS measurements," *J. Wind Eng. Ind. Aerod.*, **99**, 682-690

5. COST Action 732, *Best practice guideline for the CFD simulation of flows in the urban environment*, Cost Office

6. Davenport, A. (1964), "Note on the distribution of the largest value of a random function with application to gust loading," Proceedings of the Institution of Civil Engineers, **28(2)**, 187-196

7. Franke, J., Hellsten, A., Schlunzen, K. H., and Carissimo, B. (2011). "The COST 732 Best Practice Guideline for CFD simulation of flows in the urban environment: a summary." *International Journal of Environment and Pollution*, **44(1–4),** 419– 427

8. Ha, Y.-C. (2021). *Wind Resistant Design on Buildings*. (in Korean)

9. Huang, G., and Chen. X. (2007), "Wind load effects and equivalent static wind loads of tall buildings based on synchronous pressure measurements", *Engineering Structures*, **29(10)**, 2641-2653

10. Kim, B. J., Lee, B. H., and Ha, Y. C. (2010), "A study on the verification of validity for pressure integration method - A comparison with HFFB technique," *J. Wind Eng. Inst. Korea*, 14(3), 169-177 (in Korean)

11. Kou, J., Zhang, W. (2017), "An improved criterion to select dominant modes for dynamic mode decomposition," *European J. of Mechanics B/Fluids*, **62**, 109-129

12. Luo, X., and Kareem, A. (2021), "Dynamic Mode Decomposition of Random Pressure Fields over Bluff Bodies", *J. of Engineering Mechanics*, **147(4)**,

13. Park, S., and Yeo, D. (2021), "Effects of aerodynamic pressure tap layout and resolution on estimated response of high-rise structures: A case study", *Engineering Structures*, **234**, 11811

14. Peng, X., Yang, L., Gavanski, E., Gurley, K., and Prevatt, D. (2014), "A comparison of methods to estimate peak wind loads on buildings", *Journal of Wind Engineering and Industrial Aerodyanmics*, **126**, 11-23

15. Ricci, M., Patruno, L., Kalkman, L., Miranda, S., and Blocken, B. (2018), "Toward LES as a design tool: Wind loads assessment on a high-rise building", *J. Wind Eng. Ind. Aerod.,* **180**, 1-18

16. Rice, S. O. (1945), "Mathematical analysis of random noise," *Bell Tech.,* **19**, 46

17. Rusdin, A. (2017). "Computation of turbulent flow around a square block with standard and modified k-ε turbulence models", *International Journal of Automotive and Mechanical Engineering*, **14(1)**, 3938–3953.

18. Schmid, P. J. (2010), "Dynamic mode decomposition of numerical and experimental data," *J. Fluid Mech.*, **656**, 5-28.

19. Tamura, T., Nozawa, K., and Kondo, K. (2008), "AIJ guide for numerical prediction of wind loads on buildings", *J. Wind Eng. Ind. Aerod.*, **96(10-11),** 1974-1984

20. Tamura, Y., and Kareem, A. (2013). *Advanced structural wind engineering in Advanced Structural Wind Engineering.*

21. Tamura, Y., Suganuma, S., Kikuchi, H., and Hibi, K. (1999), "Proper orthogonal decomposition of random wind pressure field", *J. of Fluids and Structures*, **13(7-8)**, 1069-1095

22. Tamura, Y. (2012), *Aerodynamic database for high-rise buildings.* Tokyo: Global Center of Excellence Program, Tokyo Polytechnic Univ.

23. Thordal, M. S., Bennetsen, J. C., Capra, S., and Koss, H. H. H. (2020), "Towards a standard CFD setup for wind load assessment of high-rise buildings: Part 1 – Benchmark of the CAARC building" *J. Wind Eng. Ind. Aerod.*, **205**, 104283

국 문 초 록

전산유체역학을 이용한 초고층 건물의 풍하중과 풍응답 산정에 관한 연구

전산유체역학(CFD)은 건물 주변의 바람 흐름을 계산하고 건물에 작용하는 풍하중을 계산할 수 있는 강력한 도구이다. 최근 컴퓨터 성능과 전산유체역학 모델의 발전에 따라 초고층 건물 설계에 활용 가능성이 증가하였으나, 아직 그 정확도에 대한 검증이 부족하고 풍하중 산정에 활용하기 위한 연구가 부족하여 활용이 미미한 상황이다. 이 연구에서는 초고층 건물에 대한 CFD 해석을 통해 건물에 작용하는 풍하중을 구한 후 풍동실험과 그 결과를 비교하였다. 얻어낸 풍하중의 시간데이터로부터 건물의 풍응답을 해석하였고, 이로부터 피크 응답과 설계풍하중을 구한 후 그 값을 비교하였다. 분석 결과, 풍하중의 특성은 CFD 해석을 통해 도출할 수 있었으나, 정확한 풍하중의 산출에 있어서는 건물 모서리에서의 와류 방출 해석의 불안정성 등 아직 해결해야 할 부분이 있는 것으로 드러났다. 추가적으로, 풍압실험의 데이터 보완을 위한 CFD의 활용 가능성을 분석하였다. 풍하중이 풍압에서 적분되는 과정에서 발생하는 특성을 상관계수와 스펙트럼 분석으로 접근하였고, 데이터 수집 시 풍압을 얻어내는 지점의 위치와 개수에 의한 영향을 분석하였다. 이를 통해 풍압공의 개수가 제한되어 있는

풍압실험의 정확도를 CFD 해석을 활용하여 향상시킬 수 있는
것으로 나타났다.

핵심용어: 전산유체역학, 풍하중 산정, 초고층
학번: 2021-25117